JAERI-M
7 6 1 0

RECENT RESULTS IN THE DIVA EXPERIMENT

March 1 9 7 8

DIVA Group

Division of Thermonuclear Fusion Research

日 本 原 子 力 研 究 所
Japan Atomic Energy Research Institute

Recent Results in the DIVA Experiment

DIVA Group[*]

Division of Thermonuclear Fusion Research,

Tokai Research Establishment, JAERI

DIVA (JFT-2a) is a small tokamak having an axisymmetric divertor with the toroidal magnetic field increased to 2 T from 1 T. Divertor effects on impurities, radiation loss and plasma-confinement, characteristics of a scrape-off layer plasma, impurity shielding by a scrape-off layer plasma and mechanism of metallic impurity release have been studied over a wide range of plasma parameters: electron temperature T_{eo} = 200–700 eV, ion temperature T_{io} = 60–300 eV and density n_{eo} = (1.5–8.0)x10^{13}cm^{-3} in the main plasma, and T_{es} = 20–100 eV, T_{is} = 20–60 eV and n_{es} = (1.5–5.0)x10^{12}cm^{-3} in the scrape-off layer plasma. The following results are obtained.

1) The divertor reduces plasma-wall interactions near the main plasma by guiding loss plasma into the divertor chamber. A maximum divertor efficiency is 35 % for particle flux and 75 % for heat flux.

2) The scrape-off layer plasma shields impurity influx, guides ionized impurities into the divertor, and reduces influx of injected impurities into the main plasma by a factor of 2–4. Shielding efficiency is higher for alminum than for carbon. Shielding effect is also observed in a conventional discharge.

3) The divertor reduces radiation loss by a factor of 2–4 and hence increases the energy-confinement time by a factor of 2.5.

4) The divertor does not significantly affect particle-confinement time, ion temperature and heat diffusion coefficient.

5) The radiation loss due to pseudo continuum mainly from gold ions is comparable to that due to oxygen lines. Impurity confinement time is comparable to the average particle-confinement time.

6) The particle flow velocity is a few times less than the sound velocity, the heat transmission rate is consistent with a sheath model, and the particle diffusion coefficient in the scrape-off layer is about ten times less than the Bohm diffusion coefficient. Scaling for electron temperature is obtained.

7) Ion sputtering, arcing and evaporation are identified. The ion sputtering by impurity ions is the dominant process of metallic impurity release from a limiter or a neutralizer plate in a stable discharge.

Key Words: DIVA, Axisymmetric divertor, Impurity radiation loss, Metallic impurity, Divertor efficiency, Scrape-off layer plasma, Plasma confinement, Pseudo continuum, Ion sputtering, Arcing, Evaporation.

DIVA 実験の最近の結果

日本原子力研究所東海研究所核融合研究部
DIVA グループ

DIVA（JFT-2a）は軸対称ダイバータを有する小型トカマク装置であり，そのトロイダル磁場は 1 T から 2 T に増力された。不純物・輻射損失・プラズマ閉じ込めへのダイバータの影響，スクレイプ・オフ層プラズマの性質および金属不純物の発生原因についての研究を下記の広いプラズマ・パラメータ範囲にわたって行なってきた。（主プラズマにおいて，電子温度 $T_{eo} = 200 - 700$ eV，イオン温度 $T_{io} = 60 - 300$ eV，密度 $n_{eo} = (1.5 - 8.0) \times 10^{13}$ cm^{-3}。スクレイプオフ層において，$T_{es} = 20 - 100$ eV，$T_{is} = 20 - 60$ eV，$n_{es} = (1.5 - 5.0) \times 10^{12}$ cm^{-3}。）下記の結果を得た。

1）ダイバータは，損失プラズマをダイバータに導びくことによって，主プラズマ近傍でのプラズマと壁との相互作用を低減する。ダイバータ効率の最大値は，粒子に対して 35 ％，熱に対して 75 ％である。

2）スクレイプ・オフ層プラズマは流入不純物をしゃへいし，電離した不純物イオンをダイバータに導びき，入射不純物の主プラズマへの混入量を 1／2 に減ずる。

3）ダイバータは不純物による輻射損失を 1／4 ～ 1／2 に減少し，その結果，エネルギ閉じ込め時間を 2.5 倍に増加する。

4）ダイバータは，粒子閉じ込め時間，イオン温度，熱拡散係数には影響を与えない。

5）金からの擬似連続による輻射損失は酸素の線スペクトルによる輻射と同程度である。

6）スクレイプ・オフ層において粒子の流速は音速の数分の 1，熱伝達率はシースモデルから予想される値にほぼ等しく，粒子拡散係数はボーム拡散の約 1／10 である。

7）イオン・スパッタリング，アーキング，蒸発がそれぞれ見分けることができた。安定な放電では，不純物イオンによるスパッタリングが，金属不純物の主要な発生原因である。

Contents

目　　次

1. Introduction

It is generally believed that some method of impurity control will
be required to obtain thermonuclear plasma in a tokamak device. In order
to control impurities, it is necessary to control impurity production at the
vacuum surface, impurity influx into the main plasma and impurity outflux
from the main plasma. The divertor is one of promising methods controlling
impurities and divertor tokamaks have been studied.[1)~3)] The important
divertor actions are summarized as follows:

a) Plasma insulation from the first wall.

A divertor guides a loss plasma from the main chamber into the
burial chamber and moves a surface contacting with a plasma from a
limiter to a remote neutralizer plate. Consequently, plasma-wall
interactions and impurity production are removed from a limiter surface
to the burial chamber. Some portion of impurities produced in the divertor
chamber may flow into the main plasma. In the divertor chamber, however,
plasma-wall interactions are more easily controlled than near the main
plasma.

b) Shielding impurity influx.

Impurity particles proceeding to the main plasma column can be ionized
in a scrape-off layer plasma flowing into the divertor chamber. Ionized
impurities may be acceralted by space potential and the scrape-off layer
plasma and/or spread by their own thermal motion into the burial chamber
along magnetic field lines.

Another divertor action will not be discussed in this paper is "pumping-
out fuel particles and impurities including α-particles". By pumping-out
and suppressing back flow of fuel particles, the divertor can reduce
neutral particles in the main plasma and reduce high energy charge-
exchange particles which sputter out wall material. The plasma density,
however, decreases during the particle-confinement time without fueling
and it seems very difficult to fuel without producing neutral particles.
The back flow of impurities are also reduced with a pumping system in the
divertor. Metallic impurities stick naturally on the divertor chamber
wall and gaseous impurities are essentially reduced by cleaning the vacuum
wall as observed in experiments. Therefore, an artificial pumping system
is not necessary for impurities in the divertor chamber. α-particles,
however, has to be pumped out from a reactor to maintain a reactor plasma
with a constant fraction of α-particles. The fraction of the total particle

loss flux from the reactor plasma which has to be pumped out is estimated
small assuming the same particle-confinement time for fuel particles and
α-particles because the burning time is much longer than the particle confine-
ment time as discussed in ref.4. From these discussions, pumping-out of
guided fuel and impurities are less important in the divertor. Therefore,
the main objective of divertor experiments is to clarify dynamics of plasma
insulation from the first wall and shielding impurity influx and offers data
from which we can discuss impurity control in a future large tokamak.

One of the most important divertor experiments is demonstration of
impurity reduction by reducing plasma-wall interactions and shielding
impurity influx. Up to now, the results show that impurities are reduced
by both of an axisymmetric divertor in DIVA[5)6)] and a bundle divertor in
DITE.[2)7)8)] In both devices, however, only a low power discharge with a
low temperature and low density plasma has been investigated, i.e. ohmic
power input $p_{in} \sim 50$ kW, center electron temperature $T_{eo} \sim 300$ eV, ion temper-
ature $T_{io} \sim 80$ eV and density $n_{eo} \sim 1.5 \times 10^{13}$ cm^{-3}. Therefore, impurity control
has to be investigated over a wide range of plasma parameters. Another
important study is to understand divertor effects on plasma-confinement. A
divertor has both possibility to improve plasma-confinement by reducing
radiation loss and to increase radial transport of a confined plasma by
deforming magnetic configuration. Improvement of energy-confinement time
is briefly discussed in ref. 6 but divertor effects on other plasma parameters
have not been investigated. Therefore, it is also necessary to study the
divertor effects on the plasma confinement in more detail.

Preliminary experiment of shielding was done in DITE[2)]. However,
impurity flow into the divertor and shielding efficiency were not investigated.
For direct observation of shielding action, spectroscopic measurements are
necessary not only in the main chamber but also in the burial chamber.

Quantitative understanding and generalization of divertor actions are
necessary to discuss impurity control in a future large tokamak. Divertor
actions, i.e. plasma insulation from the first wall and shielding impurity
influx are ruled by a scrape-off layer plasma which also rules the plasma-
wall interactions in the burial chamber and impurity flow from the divertor
chamber. This situation does not change in a conventional tokamak except
that a surface contacting with a plasma is not a remote neutralizer plate
but a limiter. From this point of view, investigation on a scrape-off layer
plasma is needed in a divertor device and also in a conventional tokamak.

Plasma parameters in a scrape-off layer, i.e. electron temperature T_{es}, width of a scrape-off layer d, density n_{es}, particle flux density f_p and heat flux density q, are roughly given as follows:

$$\bar{T}_{es} = \frac{3\bar{\tau}_p (P_{in} - P_{cx} - P_R)}{2\tau_E \ P_{in}\gamma}(\bar{T}_e + \bar{T}_i) \qquad (1-1)$$

$$d = \sqrt{D_\perp L/v_f} \qquad (1-2)$$

$$\bar{n}_{es} = \frac{L\bar{n}_e a}{2v_f\bar{\tau}_p d} \qquad (1-3)$$

$$f_p = n_{es} \ v_f \qquad (1-4)$$

$$q = \gamma T_{es} \ f_p \qquad (1-5)$$

γ, $D_\perp$, v_f and L are heat transmission rate, diffusion coefficient, particle flow velocity, and half length of a magnetic field line between material surfaces in scrape-off layer, respectively, and P_{in}, P_{cx}, P_R, τ_p, τ_E, T_e, T_i, n_e and a are input power, charge-exchange loss-power, radiation loss-power, particle-confinement time, energy-confinement time, electron temperature, ion temperature, density and minor radius in a main plasma column, respectively. $\bar{T}_{es}$, d, $\bar{n}_{es}$, f_p and q can be calculated from these equations if we know v_f, γ and $D_\perp$ with assuming a main plasma. Space potential and floating potential which are also important parameters can be also estimated from these values assuming a magnetic configuration and secondary electron effects. Therefore, the essential parameters in a scrape-off layer plasma are v_f, γ and $D_\perp$. The particle flow velocity v_f was observed a few times less than the sound velocity c_s, i.e. typically $v_f = 0.3 \ c_s$, in FM-1 with $T_{es} = 2$ ev[9] and in DIVA with $T_{es} \approx 20$ ev.[10] The heat transmission rate γ was intensively investigated in DIVA with $T_e \approx 30$ eV (see Appendix I) and the result was $\gamma \approx 5$–15 which is consistent with a sheath model including epithermal electrons and secondary electron effects.[11] The particle diffusion coefficient $D_\perp$ was roughly ten times less than the Bohm diffusion coefficient in DIVA but the parameter dependence of D has not been clarified.[10]

Electron temperature T_{es} is very important not only in atomic process and transport process but also in impurity production because arcing is strongly affected by the electron temperature and ions accelerated by space and sheath potential can easily sputter out wall material.[12] Therefore,

a scrape-off layer plasma with a high electron temperature has to be studied. Even in a reactor, however, the edge plasma should be controlled at a rather low temperature because of the following reason. Energy of an ion at a material surface is roughly given by the following equation.

$$E = zV + T_z \qquad (1-6)$$

where z, T_z and V are the charge number, temperature of the ion and difference between space and floating potential. If we consider a limiter or a neutralizer plate made of molybdenum and T_{es} =100 eV, we obtain $S_D \sim 0.005$, $S_T \sim 0.01$, $S_{He} \sim 0.05$ and $S_I \sim 1$,[13] where S_D, S_T, S_{He} and S_I are sputtering yield for D^+, T^+, He^{++} and multi-ionized impurity-ions, respectively. In this case, wall erosion and impurity production are very serious. Arcing and evaporation are also serious in a high temperature plasma. Therefore, the edge plasma has to be cooled down to a rather low temperature, typically a value less than 100 eV, even in a reactor. From the above discussion, it seems sufficient to study a scrape-off layer plasmas whose electron temperature is around several tens electron volts.

Mechanisms of impurity production at a limiter or a neutralizer plate are also important as well as characteristics of a scrape-off layer plasma. Gaseous impurities from the absorbed gas on the vacuum surfaces are easily reduced by cleaning the surfaces as observed in experiments and impurities from wall material, usually metal, are more important than gaseous impurities. Evaporation was shown serious in a low density discharge[5], and arcing[14] and ion-sputtering[15] are proposed as the mechanisms of metallic impurity release in a normal discharge but have not been investigated in detail. Therefore, experimental studies on these processes are needed

DIVA is a small tokamak with an axisymmetric divertor and the maximum toroidal magnetic field has been increased to 2 T from 1 T. As a result, discharges are obtained over a rather wide range of plasma parameters, i.e. P_{in} = 40 - 300 kW, T_{eo} = 200 - 700 eV, T_{io} = 60 - 300 eV and n_{eo} = (1.5-8.0) × 10^{13} cm^{-3} in the main plasma, and $q \lesssim 2kW/cm^2$, T_{es} = 20-100 eV, T_{is} = 20 - 60 eV and n_{es} = (1.5-5.0)×10^{12} cm^{-3} in the scrape-off layer. With these plasma parameters, divertor effects on impurities, radiation loss and plasma-confinement, characteristics of a scrape-off layer plasma, impurity shielding by a scrape-off layer plasma and mechanisms of metallic impurity release are investigated.

In sect. 2, divertor effects on impurities, radiation-loss and plasma-confinement and characteristics of a scrape-off layer plasma, especially v_f,

γ, $D_\perp$ and T_{es}, are discussed. In Sect. 3, impurity shielding and impurity divertion are intensively studied by injecting methane and aluminum, and impurity confinement time is also studied. Spectroscopic studies on impurity contents and radiation-loss are gived in Sect. 4. Ion sputtering, evaporation and arcing are studied in Sect. 5. Summary is given in Sect. 6.

References

1) Yoshikawa, M., et al., in Processings of the Fifth International Conference on Plasma Physics and Controlled Nuclear Fusion Research, Tokyo, 1974 (IAEA, Vienna, 1975), Vol.I, P.17.

2) Paul, J.W.M., et al., in Proceedings of the Sixth International Conference on Plasma Physics and Controlled Nuclear Fusion Research, Berchtesgade, 1976 (IAEA, Vienna, 1977), Vol.II, P.269.

3) Bortnikov, A.V., et al., in Proceedings of Eighth European Conference on Controlled Fusion and Plasma Physics, Progue, 1977, (the Institute of Plasma Physics, Czechoslovak Academy of Sciences, Czechoslovakia, 1977), Vol.1, P.41.

4) Mills, R.G., in the Technology of Controlled Nuclear Fusion (proc. 2nd Topical Meeting, Richland, 1976) Vol.IV, US Energy Research and Development Administration, (1976) 1173.

5) Maeda, H., et al., in Proceedings of the Sixth International Conference on Plasma Physics and Controlled Nuclear Fusion Research, Berchtesgaden, 1976 (IAEA, Vienna, 1977), Vol.II, P.289; Maeda, H., et al., in Proceedings of the International Symposium on Plasma Wall Interaction, Jülich, 1976 (Pergamon Press, Oxford, 1977), P.537.

6) Yamamoto, S., et al., in Proceedings of Eighth European Conference on Controlled Fusion and Plasma Physics, Prague, 1977, (the Institute of Plasma Physics, Czechoslovak Academy of Sciences, Czechoslovakia, 1977), Vol.1, P.33.

7) Stott, P.E., et al., in Proceedings of the International Symposium on Plasma Wall Interaction, Jülich, 1976 (Pergamon Press, Oxford, 1977), P.39.

8) Fielding, S.J., et al., in Proceedings of Eighth European Conference on Controlled Fusion and Plasma Physics, Prague, 1977, (the Institute of Plasma Physics, Czechoslovak Academy of Sciences, Czechoslovakia, 1977), Vol.1, P.36.

9) Ando, K., et al., in Proceedings of the Fifth International Conference on Plasma Physics and Controlled Nuclear Fusion Research, Tokyo, 1974 (IAEA, Vienna, 1975), Vol.I, P.103.

10) Kimura, H., et al., Japan Atomic Energy Research Report JAERI-M 6971 (1977).

11) Kimura, H., et al., to be published in Nuclear Fusion; Kimura H., et al., Japan Atomic Energy Research Report JAERI-M 7287 (1977).

12) Ohasa, K., et al., submitted in Nuclear Fusion.

13) Scherzer, B.M.U., Behrish, R., Roth, J., in Proceedings of the Internationall Symposium on Plasma Wall Interaction, Jülich, 1967 (Pergamon Press, Oxford, 1977), P.353.

14) McCraken, G.M., et al., in Proceedings of Eighth European Conference on Controlled Fusion and Plasma Physics, Progue, 1977, (the Institute of Plasma Physics, Czechoslovak Academy of Sciences, Czechoslovakia, 1977)

15) Shimomura, Y., Nuclear Fusion 17 (1977) 626; 17 (1977) 1377

2. Divertor Experiment

In this section, general divertor studies, i.e. studies on reduction of impurities, improvement of plasma-confinement, and characteristics of a scrape-off layer plasma, are reported. The major results are following: Divertor reduces impurity contents by reducing plasma-wall interactions and shielding impurity influx. Consequently, the divertor reduces radiation loss by a factor 2-4 and increases energy-confinement time by a factor of 2.5. The divertor does not significantly affect on transport coefficients. In a scrape-off layer plasma, particle flow velocity is a few times less than the sound velocity, heat transmission rate is consistent with a sheath model, particle diffusion coefficient is about ten times less than the Bohm diffusion coefficient.

The device and diagnostic techniques are described in the following sub-section. Impurity reduction by reducing plasma-wall interactions, shielding impurity influx and improvement of plasma parameters are demonstrated in 3.2. In 3.3, the essential parameters, i.e. v_f, γ and $D_\perp$ and scaling for T_{es} are studied. Discussions and conclusions are given in the last sub-section.

2.1 Description of the Device and Diagnostic Techniques

Fig. 3.1 shows the cross-sectional view of the device. Detailed description of the device is given in Ref. (1) but the following modifications have been done: the maximum toroidal magnetic field has been increased to 2 T from 1 T, and the movable shell, titanium wires and their supports have been removed which are considered the main impurity-source in the divertor.[2] Plasma equilibrium with a separatrix magnetic surface, i.e. a divertor, is obtained in the gold coated copper shell with an opening towards the divertor hoop which carries a current I_D parallel to the plasma current I_p. The divertor configuration is obtained with $I_D/I_p > 0.7$ and the conventional configuration with $I_D/I_p < 0.7$ where the separatrix magnetic surface is located outside of the shell.[3] The value of I_D/I_p is kept constant during a discharge. The protection plates are used as a limiter in the case without the divertor and the plasma radius is kept 9 cm in both discharges with and without the divertor. No titanium is flushed in the following experiment.

In addition to conventional measurements of a main plasma such as

Thomson scattering, charge-exchange neutral-particle energy analysis, soft
X-ray energy analysis, visible, ultra-violet and vacuum ultra-violet
spectroscopy, microwave interferometry and low frequency oscillation
measurement by a PIN-diode, the following measurements are employed: 1)
spacial distribution of radiation loss including charge-exchange loss is
measured by scanning a calibrated and colimated pyroelectric detector;
2) each particle loss flux onto four sectors of the shell, three protection
plates and vacuum chamber are measured as ion saturation current onto each
surface; 3) Langmuir probes, one-directional Langmuir probes and Faraday cup
are used for measurements of electron temperature, ion temperature and
particle flow in a scrape-off layer plasma[5]; 4) heat flux into the divertor
is measured with thermoprobes[6]; 5) ion temperature of a scrape-off layer
plasma is also investigated by measuring Doppler broadenning of impurity
lines in the burial chamber.

2.2 Divertor Effects on Impurities and Plasma-Confinement

In order to study divertor effects, discharges with the divertor are
compared with those of conventional tokamak discharges. Figure 2-2 shows
oscillograms of typical discharges with and without the divertor in which
toroidal magnetic field B_T, plasma current I_p and minor radius a are
appreciable the same. The plasma density n_e is also controlled at the
appreciablly same value with five fast acting gas valves. The maximum
electron temperature and ion temperature are 700 eV and 270 eV with the
divertor, and 540 eV and 240 eV without the divertor, respectively. Radia-
tion loss P_{py} including charge-exchange loss, intensity of pseudo continuum
at 175 Å and intensity of OV-line (629.73 Å) are reduced by a factor of 2-3
by the divertor as shown in the figure. Radial profiles of the intensities
of pseudo continuum at 100 Å and oxygen lines and P_{py} are shown in Fig. 2-3,
and the profiles of electron temperature and density are shown in Fig. 2-4.
Figure 2-3 shows that the radiations are reduced over a plasma cross-section
and also that influx of oxygen is reduced by a factor of about three because
of reduction of OV-line intensity. Therefore, the divertor reduces radia-
tions from both high- and low-z impurities and also impurity influx, at least
oxygen influx.

Radiation loss power is investigated over a range of I_p = 8 - 53 kA and
B_T = 0.8 - 2.0 T. The radiation loss power is obtained from a difference
between measured loss power due to charge-exchange and radiation and the

charge-exchange loss calculated by Monte Carlo method for a cylindrical plasma. The calculated charge-exchange loss is a small portion of the total power loss due to charge-exchange and radiation. The results are summarized in Fig. 2-5 and the radiation loss has a good correlation with the plasma current or ohmic power. In conventional tokamak discharges, the radiation loss power is proportional to the plasma current as shown by closed circles in Fig. 2-5. By operating the divertor, the radiation loss power is reduced by a factor of 2-4 and is a slowly increasing function of the plasma current as shown by open circles in Fig. 2-5. The radiation loss power is effectively reduced by the divertor but the ratio of the radiation power P_R to the ohmic power P_{in} is not strongly changed because the divertor decreases the ohmic power by reducing z_{eff} and increasing electron temperature. $P_R/P_{in} = 0.3 - 0.4$ without the divertor and $P_R/P_{in} = 0.15 - 0.3$ with the divertor.

The observed reduction of the radiation loss by the divertor may be a result of lowering plasma-wall interactions and shielding impurity influx. Important parameters concerning to plasma-wall interactions are summarized in Table 2-1. The particle flux to the shell, i.e. the first wall, is reduced by a factor of 2 by the divertor. The heat flux to the divertor measured with a thermocouple probe is 55 % of the total ohmic power and heat flux by heat conduction and convection to the first wall is reduced by a factor of 8 by the divertor. The reduction of particle and heat flux to the first wall may mitigate impurity production at the first wall. Shielding impurity influx by the scrape-off layer is studied with additional methane gas injection from the farthest point from the divertor and the result is shown in Fig. 3-6. Carbon influx into the scrape-off layer ($r \gtrsim 9$ cm) is almost the same with and without the divertor but that to the main plasma is reduced by a factor 2 by the divertor. Further more increase of CIII line intensity and no increase of CII line intensity are observed in the divertor chamber but both intensities increase near the injector, i.e. the injected carbon is ionized and guided into the divertor.

The divertor reduces loop voltage V_L (Fig. 2-2) and broadenning electron temperature profile (Fig. 2-4), and consequently, the energy-confinement time increases from 1 ms to 3 ms in this discharge. In order to study the divertor effects on plasma parameters in detail, energy-confinement time τ_E, average particle-confinement time $\bar{\tau}_p$ and ion temperature T_i with and without the divertor are investigated over a wide range of plasma parameters,

i.e. toroidal magnetic field B_T=0.8 - 2.0 T, I_p=10 - 53 kA, safety factor q_a=2.6 - 5.9 and mean electron density $\bar{n}_e$=(1.5 - 5.0) × 10^{13} cm^{-3}. It is clearly shown in Fig. 2-7-a that the divertor increases the energy-confinement time by a factor of 2.5 which has the functional dependence of the ALCATOR scaling[7]) as follows: τ_E=1.5 $\sqrt{q_a}$ $\bar{n}_{14}$ ms without the divertor and τ_E=4.0 $\sqrt{q_a}$ $\bar{n}_{14}$ ms with the divertor where $\bar{n}_{14}$=10^{-14} $\bar{n}_e$. The average particle-confinement time shown in Fig. 2-7-b is calculated from the total particle loss-flux measured as the total ion saturation current onto the shell, protection plates and burial chamber. The result is contrast to that of the energy-confinement time i.e. a large improvement by the divertor is not observed on this average particle-confinement time. The average particle-replacement time is roughly given by the ALCATOR scaling for the energy-replacement time, i.e. $\bar{\tau}_p$=2.0 $\sqrt{q_a}$ $\bar{n}_{14}$ ms without the divertor and τ_p=3.0 $\sqrt{q_a}$ $\bar{n}_{14}$ ms with the divertor. The ion temperature shown in Fig. 2-7-c agrees with the Artsimovich scaling law with and without the divertor.

The divertor increases the energy-confinement time by a factor of 2.5 which seems a result of lowering the radiation loss. The radiation-loss power is not a large portion of the total energy loss, i.e. 30 - 40 % of the ohmic power without the divertor and 15 - 30 % with the divertor. Electron temperature profiles, however, are strongly affected by the radiation loss, i.e. by the divertor, as shown in Fig. 2-4. The divertor increases the radius of the hot column by reducing the radiation loss and consequently, increases the energy-confinement time because internal energy of a plasma is concentrated in the hot column.

2.3 Scrape-off Layer Plasma

A plasma guided into the burial chamber is investigated mainly by scanning probes. The maximum density is 5×10^{12} cm^{-3}. Ion temperature is obtained from a Faraday Cup and also Doppler broadenning of impurity lines and a Faraday Cup gives 60 eV and CV (2270.9 Å) and CIV (1548.2 Å) give 80 eV and 40 eV, respectively, in a discharge whose conditions are the same as those of Figs. 2-2, 2-3 and 2-4. The electron temperature is also measured with a Faraday Cup and an electron temperature profile of the main plasma column measured with Thomson scattering extends smoothly to the electron temperature in the scrape-off layer plasma, e.g. 100 eV at r=8 cm and 80 eV in the divertor. The electron temperature in a scrape-off layer plasma varies from 20 eV to 100 eV by changing the discharge conditions. Conservation of

the energy flux gives the electron temperature $\bar{T}_{es}$ in a scrape-off layer as written by equation (1-1) which is rewritten as follows:

$$\gamma\bar{T}_{es} = \frac{P_{in} - P_{cx} - P_R}{F_p} \ , \tag{2-1}$$

F_p is the total particle loss flux and is measured as the sum of ion satura-tion currents onto the shell, protection plates and vacuum chamber. $(P_{cx} + P_R)$ is measured with the pyroelectric detector. Fig. 2-8 shows the relation between measured electron temperature $\bar{T}_{es}$ near the surface which collects the main part of the heat flux and γ, $\bar{T}_{es}$ calculated from equation (2-2). The result gives $\gamma=4-10$ which extends the previous result[8] obtained in a low temperature plasma and is consistent with the estimated value from the sheath model.

The particle flux into the divertor is measured as ion saturation current onto the burial chamber. Particle flow velocity v_f is estimated a few times less than the sound velocity c_s from the particle flux to the divertor and the density profile in a scrape-off layer. This result is consistent with that from measurement of the one directional probe which gives $(0.2\sim0.5)\ c_s$. Divertor efficiency for the particle flux is defined as follows:

$$\eta_p = F_D/F_p \ , \tag{2-2}$$

F_D is the particle flux into the divertor. The measured divertor efficiency for the particle flux is shown in Fig. 2-9. The efficiency increases as increasing the plasma current and is not affected by the toroidal magnetic field. The maximum divertor efficiency is 35%. A simple model in which a point plasma source at the farthest point from the divertor is assumed in a scrape-off layer plasma gives the following equation for the particle divertor efficiency.

$$\eta_p = \mathrm{Erf}(y), \qquad\qquad y = \sqrt{\frac{\Delta^2 \ v_f}{4 \ D_\perp \ L}} \ , \tag{2-3}$$

where Erf, $D_\perp$, L and Δ are error function, diffusion coefficient and the length of a magnetic field line from the source point to the divertor throat, respectively. Assuming the Bohm type diffusion, the following equation is obtained because of $v_f \propto c_s$.

$$y^2 \propto I_p / \sqrt{T_{es}} \qquad (2-4)$$

This parameter dependence coincides with the experimental results as shown in Fig. 9. The experimental results give $\Delta \stackrel{\sim}{\sim} 1$ cm[9] and $v_f \stackrel{\sim}{\sim} 0.3$ c_s, and $D \stackrel{\sim}{\sim}$ 0.1 D_B is obtained from these values and equation (2-3). This result is also consistent with the previous experiment[5] in which parameter dependence was not investigated.

Heat flux into the divertor is also investigated and the divertor efficiency for the heat flux is defined as follows:

$$\eta_h = P_D / P_{CC} \qquad (2-5)$$

P_{CC} is the total loss power by conduction and convection, i.e. $P_{CC} = P_{in} - P_{cx} - P_R$, and P_D is the heat flux into the divertor and measured by scanning the thermoprobe. P_{CC} is calculated from ohmic power and $(P_{cx} + P_R)$ measured with the pyroelectric detector. The result shows that η_h is a few times larger than η_p. Typical power balance and particle balance with and without the divertor are shown in Table 1. In this case, 33 % of the total particle loss and 75 % of conduction and convection loss are guided into the divertor, i.e. $\eta_p = 0.33$ and $\eta_h = 0.75$.

Relation between energy-confinement time τ_E and average particle confinement-time $\bar{\tau}_p$ is also important for a scrape-off layer plasma and is shown in Fig. 2-10. In a conventional discharge, $\bar{\tau}_p / \tau_E \stackrel{\sim}{\sim} 1.5$. By operating the divertor, τ_E increases and $\bar{\tau}_p$ dose not strongly change. Consequently, the ratio decreases and $\bar{\tau}_p / \tau_E \stackrel{\sim}{\sim} 0.8$.

2.4 Discussions and Conclusions

The results show that the divertor reduces the radiation loss by a factor of 2-4. This is the same effect observed in the previous experiment[2],[9] in which a low-z free plasma was obtained[10] and the radiation loss was mainly due to pseudo continuum. The pseudo continuum was observed only in the range of 120 Å - 250 Å in the previous experiment with a low temperature plasma[11] (see Appendix II) and is observed in the range of 45 Å - 250 Å in these experiments. This is reasonable because electron temperature increases from 250 eV to several handred electron volts by increasing the toroidal magnetic field. The pseudo continuum is considered due to gold because it

increases as inserting a gold plate into the plasma and has a good correlation with AuI- and AuII-lines. Profiles of the total radiation loss, radiation from oxygen and radiation of pseudo continuum show that the radiation loss by oxygen is the same order as that of the pseudo continuum (Fig. 2-3). This experiment was done during the first few months after completing the modifications which forced to open the vacuum vessel to the atmosphere for a few months and low-z impurities can not be neglected. Influx of oxygen is reduced by a factor of about 3 because intensity of OV-line decreases by a factor of 3 with the divertor (Fig. 2-3). It is suggested that oxygen content is also reduced by the divertor because oxygen influx is decreased and confinement-time of oxygen is roughly equal to the particle confinement-time (see sub-section 3) which is not strongly affected by the divertor as shown in Fig. 2-7-b. The divertor reduces gold content at least by a factor of three because radiation loss due to gold decreases by a factor of 3 (Fig. 2-3) and increases monotonically as increasing electron temperature from 200 eV to 1000 eV from calculated results.[12] Effective ionic charge number is estimated 5 without the divertor and 3 with the divertor from plasma resistivity and temperature profiles. Therefore, the divertor reduces not only the radiation loss but also impurity content. Absolute measurements of impurity content and transport, however, are needed for a detailed discussion.

Reduction of impurities is a result of lowering plasma-wall interactions and shielding impurity influx by the divertor. The divertor efficiency increases as increasing the plasma current as shown in Fig. 2-9 and consequently, radiation loss is reduced more significantly in a high current discharge as shown in Fig. 2-5. In order to understand dynamics of the divertor actions, it is necessary to know plasma-wall interactions and analyze impurity transport in a scrape-off layer.

The divertor increases the energy-confinement time by a factor of 2.5. This seems a result of broadenning the electron temperature by reducing the radiation loss. The electron temperature profile is significantly affected by the radiation loss and also by the saw-tooth oscillations in an ohmically heated plasma. In low-q discharge, i.e. around q_a=3, the amplitude of the saw-tooth oscillations increases as increasing the plasma current and the temperature profiles become broad as observed in other conventional tokamaks. In order to eliminate this effect, two electron profiles with and without the divertor are investigated in discharges with small saw-tooth oscillations. Calculated heat-diffusion coefficient from these profiles is about

4×10^3 cm^2/s without the divertor and about 3×10^3 cm^2/s with the divertor. This small difference in the heat-diffusion coefficient is consistent with the conclusion, i.e. the divertor increases the energy-confinement time by increasing the effective radius. Ion temperature and particle-confinement time are not significantly affected by the divertor. These results show that the divertor affects a plasma by reducing radiation loss not by changing transport coefficient.

Divertor effects on mhd characteristics are also important. Sawtooth oscillations are observed in both discharges with and without the divertor. The amplitude with the divertor is smaller than that without the divertor in the same discharge conditions and this seems a result of the different in the electron temperature profiles. In the previous experiment[13] with B_T=1 T, negative spikes in the loop voltage preceded by m=2 precusor fluctuations were observed in discharges with $q_a \lesssim 3.5$ where q_a is the safety factor in a circular cross-sectional tokamak with the same major radius and the same minor radius. In a higher field operation with B_T=2 T, no negative spike was observed in diverted discharges with $q_a \gtrsim 2.6$. Unfortunately, a higher current discharge has not been investigated with the divertor because of saturation of the iron transformer.

Scrape-off layer plasma and relation between particle-confinement time and energy-confinement time are investigated and the following results are obtained: $v_f \approx 0.3 \ c_s$, $\bar{\tau}_p/\tau_E \approx 1$, $D_\perp \approx 0.1 \ D_B$ and $\gamma \approx 7$. Thus, equation (1-1) is simplified as follows:

$$\bar{T}_{es} \approx 0.2 \ \frac{(P_{in} - P_{cx} - P_R)}{P_{in}} \ (\bar{T}_e + \bar{T}_i) \qquad (2-6)$$

This equation shows that temperature at the edge is extremely high in a high temperature tokamak with $P_{in} \gg P_{cx} + P_R$, and surface erosion and impurity production become serious. Thus, some method is necessary to cool the edge plasma down to a sufficient low temperature, typically several tens electrons volts, as discussed in Ref. 14. The other important parameters, i.e. the line density of a scrape-off layer plasma $\bar{n}_{es} \ d$, is given by assuming device parameters. For example, the following parameters, are assumed: R=5 m, a=1.5 m, $\bar{n}_e$=6 × 10^{13} cm^{-3}, $\bar{\tau}_p$=1 s, an ideal poloidal limiter and $\bar{T}_{es}$=50 eV with some cooling method. The line density is about 1×10^{13} cm^{-2}. This value is sufficient high to shield the impurith influx because shielding effect by a plasma with a lower line-density, i.e. $\bar{n}_{es} \ d$

$\lesssim 5 \times 10^{12}$ cm^{-2}, is observed in the experiment but seems too low to shield the hydrogen influx because the charge-exchange process and the wall reflection give a high energy for the neutral particles.[15]

Concluding this section, reduction of impurities and improvement of plasma-confinement by the divertor are demonstrated over a rather wide range of plasma parameters. These divertor effects are a result of lowering plasma-wall interactions and shielding impurity influx. Particle flow, heat flow and diffusion are invesrigated in a scrape-off layer plasma with $T_{es}=$ 20 - 1000 eV and the results are very similar to those in the previous experiment with a low temperature plasma. An empirical scaling of T_{es} is obtained.

References

1) Shimomura, Y., et al., Japan Atomic Energy Research Institute Report JAERI-M 6102 (1975).

2) Maeda, H., et al., in Proceedings of the Sixth International Conference on Plasma Physics and Controlled Nuclear Fusion Research, Berchtesgaden, 1976 (IAEA, Vienna, 1977), Vol.II, P.289; Maeda, H., et al., in Pro Proceedings of the International Symposium on Plasma Wall Interaction, Jülich, 1976 (Pergamon Press, Oxford, 1977), P.537.

3) Shimomura, Y., Ohtsuka, H., Maeda, H., Yamamoto, S., Kimura, H., Nagami, M., and Ueda, N., Nuclear Fusion 16 (1976) 587.

4) Odajima, K., et al., to be published in Nuclear Fusion.

5) Kimura, H., et al., Japan Atomic Energy Research Report JAERI-M 6971 (1977).

6) Seki, M., Kawamura, H., Ueda, N., Maeda, H., Journal of Nuclear Science and Technology, 14 (1977) 68.

7) Apgar, E., Coppi, B., Condlhalker, A., Helava, H., Komm, D., Martin, F., Montogomery, B., Pappas, D., Parker, R., and Overskei, D., in Proceedings of the Sixth International Conference on Plasma Physics and Controlled Nuclear Fusion Research, Berchtesgaden, 1976 (IAEA, Vienna, 1977), Vol.I, P.247.

8) Kimura, H., et al., to be published in Nuclear Fusion; Kimura H., et al., Japan Atomic Energy Research Report JAERI-M 7287 (1977).

9) Yamamoto, S., et al., to be published in Nuclear Fusion.

10) Nagami, M., et al., to be published in Nuclear Fusion.

11) Shiho, M., et al., Japan Atomic Energy Research Institute Report

JAERI-M 7397 (1977).

12) Post, D.E., Jensen, R.V., Tarner, C.B., Grasberger, W.H., Loke, W.A., Princeton Plasma Physics Laboratory Report PPPL-1352 (1977).

13) Shimomura, Y., et al., Physics of Fluids $\underline{19}$ (1976) 1635.

14) Shimomura, Y., Nuclear Fusion $\underline{17}$ (1977) 626; Shimomura, Y., Nuclear Fusion $\underline{17}$ (1977) 1377.

15) Fielding, S.J., McCraken, G.M., Erents, S.K., Pospieszczyk, A., Stott., P.E., in Proceedings of Eighth European Conference on Controlled Fusion and Plasma Physics, Progue, 1977, (the Institute of Plasma Physics, Czechoslovak Academy of Sciences, Czechoslovakia, 1977), Vol.I, P.39; Wagner, F., Mayer, H.M., ibid, Vol.I, P.24.

Table 1. Particle flux and heat flux[+]

Divertor	Particle Flux $(10^{18}$ ms$^{-1})$		Heat Flux (kW)			
			Conduction and Convection		Radiation	Charge-Exchange
	Divertor	Limiter and Wall	Divertor	Limiter and Wall		
off	0	2.1	0	200	102	10
on	0.5 (33 %)	1.0	75 (55 %)	25	30	10

+ Discharge conditions are the same as shown in Fig. 2-2.
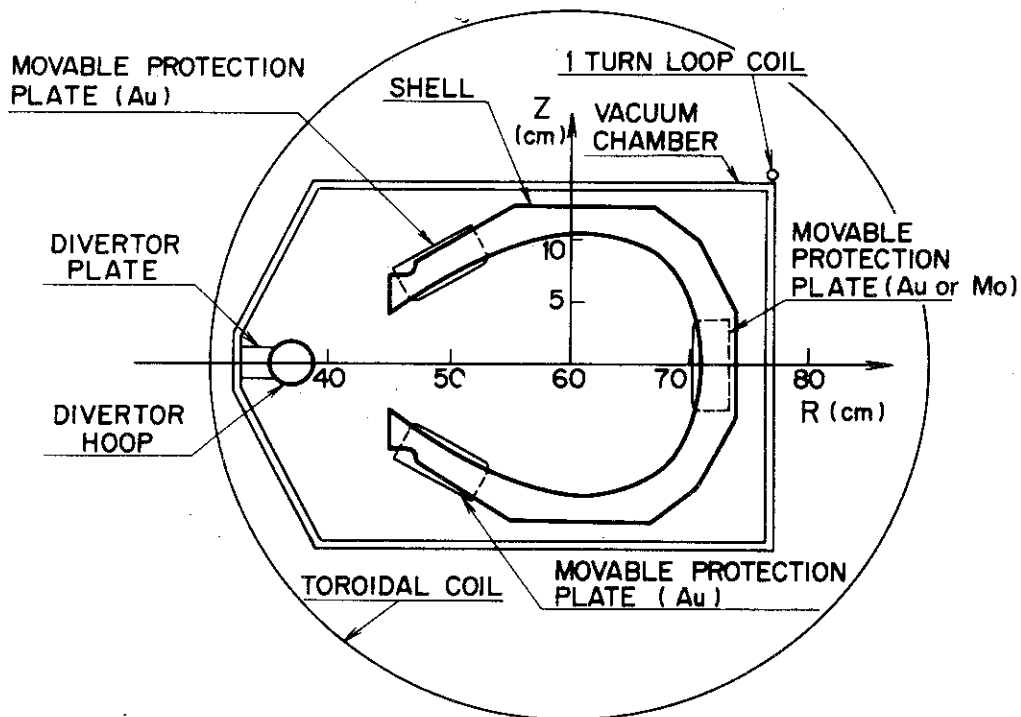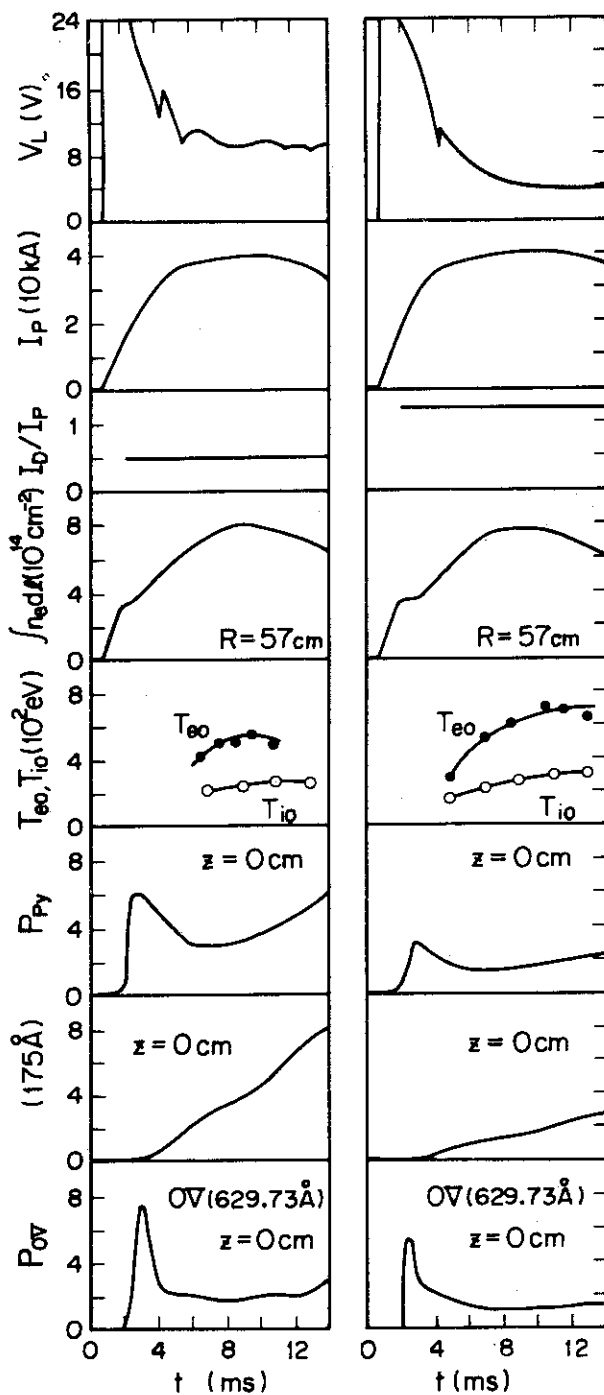

Fig. 2-1 Cross-sectional view of DIVA

Fig. 2-2 Time behaviours of plasma parameters with the divertor (right side) and without the divertor (left side). V_L: loop voltage, I_p: Plasma current, I_D/I_p: ratio of divertor coil current to plasma current, $\int n_e \, d\ell$: line density, T_{eo}: center electron temperature, T_{io}: center ion temperature, P_{py}: loss power due to charge-exchange and radiation, intensity of pseudo continuum at 175 Å and P_{ov}: intensity of OV-line (629.73 Å). Toroidal magnetic field is 2T.
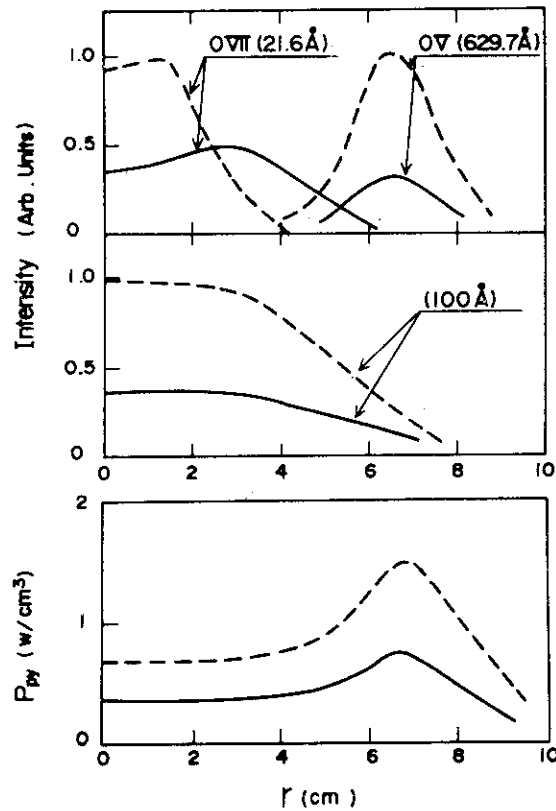
Fig. 2-3 Radial profiles of intensities of OVII (21.6 Å), OV (629.7 Å)
and pseudo-continuum at 100 Å and power loss P_{py} due to
charge-exchange and radiation with the divertor (——) and
without the divertor (----) at 9 ms. The discharge
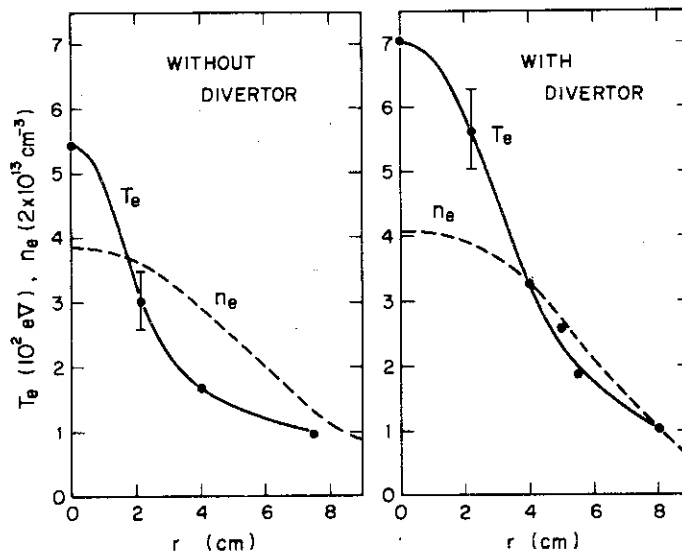conditions are the same as shown in Fig. 2-2.

Fig. 2-4 Radial profiles of electron temperature (——) and density
(----) with and without the divertor at 9 ms. The
discharge conditions are the same as shown in Fig. 2-2.
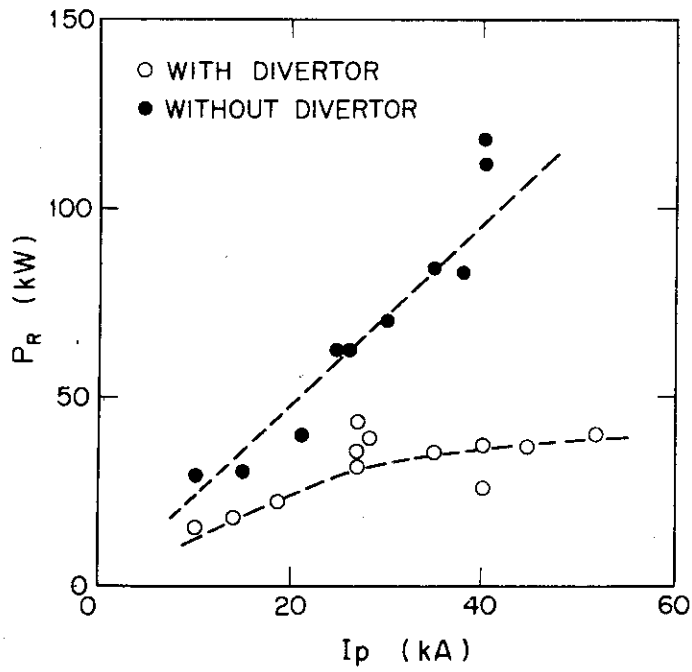
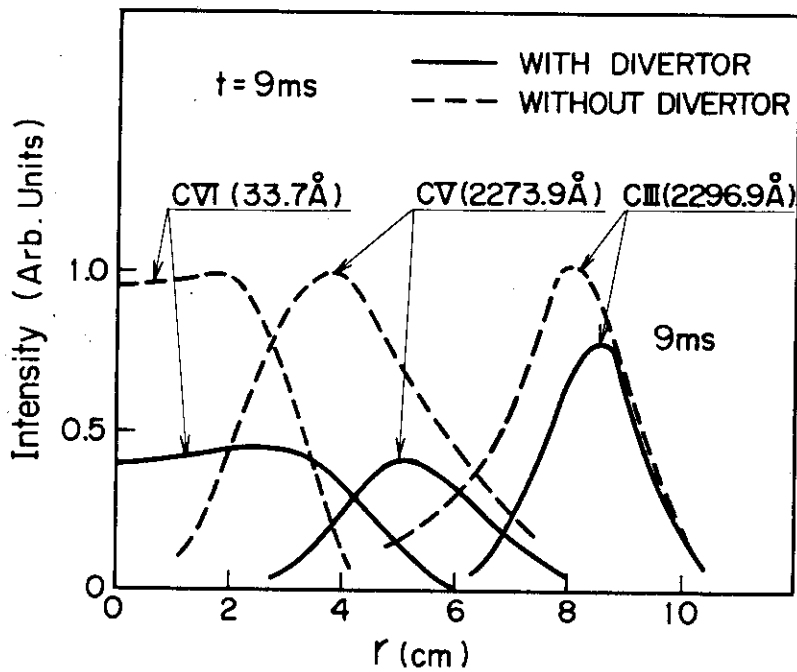Fig. 2-5   Radiation loss power vs. plasma current I_p.

Fig. 2-6   Radial profiles of line emission by increased carbon at 3 ms
after injecting methane gas with and without the divertor.
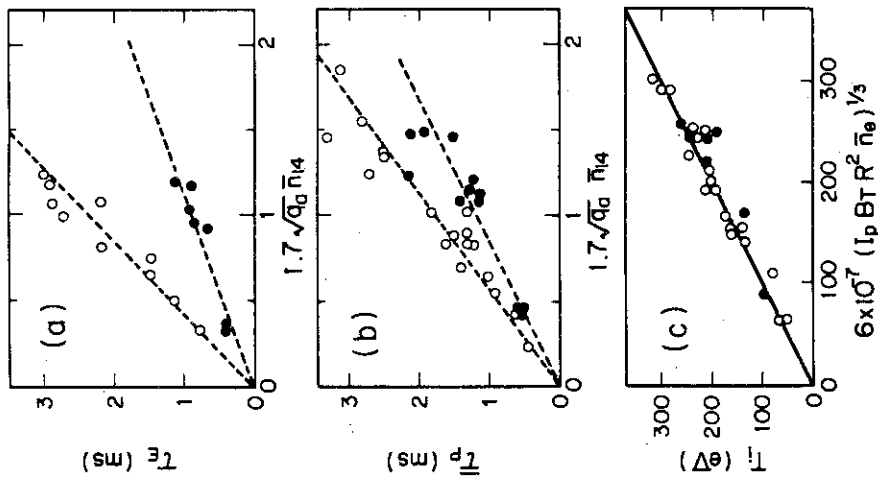The discharge conditions are the same as shown in Fig. 2-2.

$$\left(\gamma \overline{T}es = 1.5 \times \frac{\overline{\tau}_P}{\tau_E} \frac{P_{in} - P_{cx} - P_R}{P_{in}} (\overline{T}_i + \overline{T}_e) \right.$$

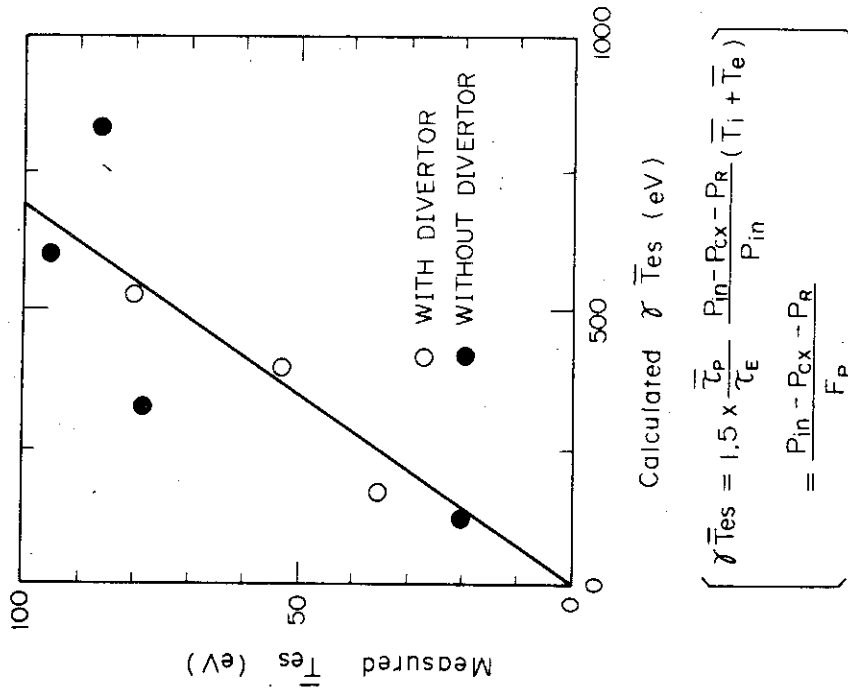$$\left. = \frac{P_{in} - P_{cx} - P_R}{F_P} \right)$$

Fig. 2-8 Measured electron temperature $\overline{T}$ in scrape-off layer plasmas and es calculated $\gamma\overline{T}_{es}$ from equation (2-1).

Fig. 2-7 Energy-confinement time τ_E, average particle-confinement time $\overline{\tau}_p$ and central ion temperature T_i with the divertor (o) and without the divertor (•). I_p: plasma current, q_a: safety factor, $\overline{n}_{14} = \overline{n}_e / (10^{14} \text{ cm}^{-3})$ and $(I_p B_T R^2 \overline{n}_e)$ in (A·G·cm²·cm⁻³).
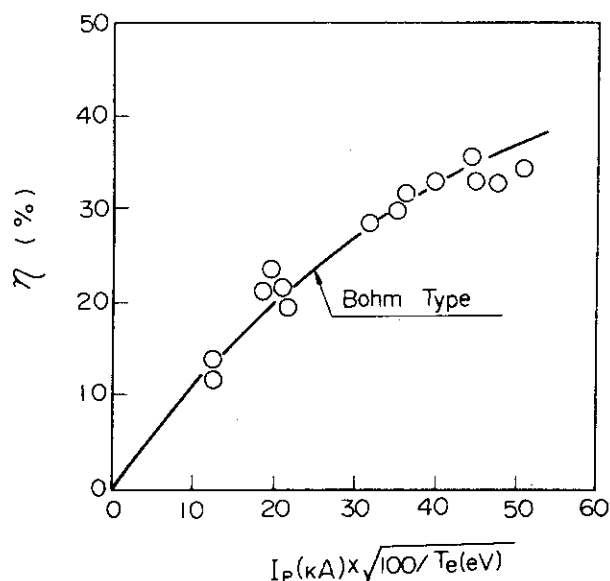
Fig. 2-9 Particle divertor efficiency η_p. $B_T=0.8+2.0$ T, $n_{es}=(1.5-5.0)\times 10^{12}$cm^{-3} and $T_{es}=20-100$ eV.
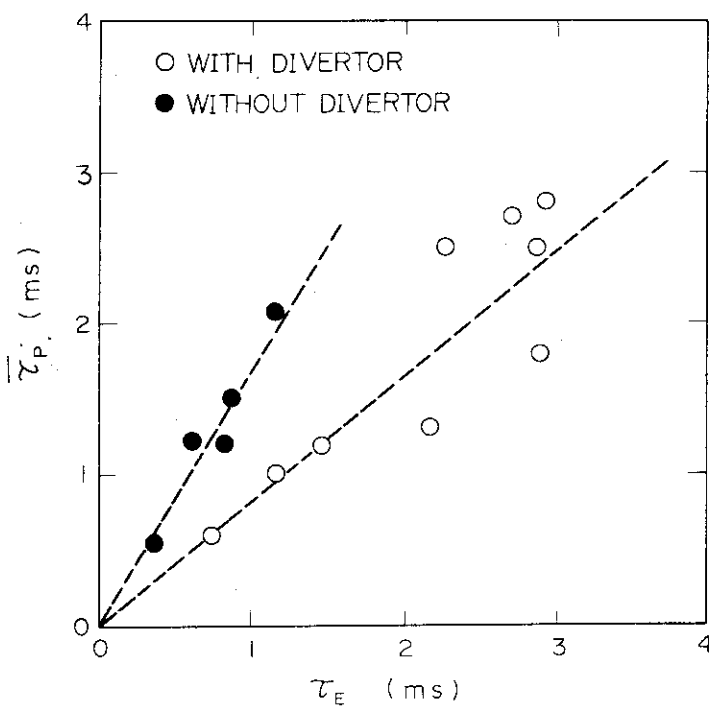

Fig. 2-10 Relation between the average particle-confinement time $\bar{\tau}_p$ and the energy-confinement time τ_E with and without the divertor. $B_T=0.8-2.0$ T, $I_p=10-53$ kA, $q_a=2.6-5.9$, $\bar{n}_e=(1.5-5.0)\times 10^{13}$ cm^{-3}, $T_{i0}=80-300$ eV and $T_{e0}=200-700$ eV.

3. Shielding Impurity Influx and Sweeping-out Impurity Ions by Scrape-off Layer Plasma

One of the most important aspects of divertor operation is impurity shielding by the scrape-off plasma. Impurity atoms that originate from the vacuum chamber wall are ionized in the divertor scrape-off and the resultant impurity ions are swept into the burial chamber by the escaping plasma. One of the other important action is sweeping-out of the impurities diffused from the main plasma into the remote burial chamber. By this action, impurity recycling and plasma-wall interaction can be reduced in the main vacuum chamber.

The shielding action against injected impurity was studied in DITE with the bundle divertor[1]. They find an increment of loop voltage by a factor of 4.5 with a non-diverted discharge, although the loop voltage is not changed in a diverted discharge for puffing the same amount of oxygen. However impurity flow into the remote burial chamber and the comparison of the accumulation of injected impurity in the main plasma with the spectroscopic measurement are beyond the scope of this experiment.

In this section, these fundamental divertor actions on the impurity are discussed. We have injected a pulse of methane gas and a short burst of aluminum into DIVA plasma at the farthest point from the divertor. For the same amount of impurity injection, the accumulation of the injected impurity in the main plasma is reduced by factor 2-4 by the divertor action. The impurity shielded by the scrape-off plasma is rapidly guided into the burial chamber. The excursion time into the burial chamber is equal to the flow time of the scrape-off plasma. Sweeping-out the impurity ions diffused from the main plasma into the burial chamber is also distinguished. Impurity transport in a scrape-off layer and impurity continement time are also investigated.

In this paper fundamental divertor actions on the impurity mentioned above are studied for DIVA tokamak with an axisymmetric poloidal divertor. By employing pulsed methane gas and aluminum injection, and in conjunction with visible and vacuum ultraviolet spectroscopies, the transport of the injected carbon ions along and across the scrape-off field lines are studied.

In sub-section 3.1, the experimental arrangement is presented. In sub-section 3.2, the comparison of the accumulation of the injected impurity in discharges with and without divertor are presented. In sub-

section 3.3, observation of parallel flow of the injected impurity ions along the scrape-off field lines is presented. In sub-section 3.4, discussions and conclusions are given.

3.1 Experimental Set-up and Discharge Conditions

DIVA is a tokamak with an axisymmetric divertor. Detailed description of the device is given in Ref.[2] In the present experiment, the toroidal field is fixed at 20 kG and no titanium is flushed in the burial chamber.

Fig. 3.1 shows the positions of CH_4 and aluminum injection and the arrangement of three monochromators.

The monochromator system 1 (M.1) consists of; 1) a 3 m grazing incidence vacuum monochromator calibrated by means of the atomic branching ratio method, and 2) a visible and uv monochromator calibrated by means of a standard tungsten ribbon lamp and a NBS-uv hydrogen discharge standard lamp. In a section placed 45° from the gas inlet in the toroidal direction, this system allows a shot-to-shot vertical scanning with the space resolution of 1 cm (vuv) and 1.6 cm (visble and uv).

The monochromator 2 (M.2) is a non-calibrated 1 m Czerny-Terner type vacuum monochromator, which is placed 135° from the gas inlet. By scanning an aluminum mirror horizontally, line emission from plasmas in the burial chamber and in the inner half of the main plasma is measured with a space resolution of 2 cm.

To make easy in comparing the accumulation of injected impurity, the discharges with same electron temperature and electron density is desirable. However, in a discharges with a same plasma current, toroidal field and the average electron density, the electron temperature are much different in discharges with and without divertor, i.e. the divertor increases the maximum electron temperature and broadens the temperature profile. Therefore, the plasma current with the divertor is kept lower than that without the divertor and following discharge conditions are employed: plasma current I_p is 30 kA, ratio of divertor hoop current to the plasma current I_D/I_p is 1.56, and for non-diverted discharge I_p=40 kA, I_D/I_p=0.46.

Figure 3.2 shows time behaviors of I_p, loop voltage V_L and line integrated electron density at R=60cm in discharges with and without the divertor. Figure 3.3 shows radial profiles of electron temperature and density. The peak ion temperature in both discharges are about 200 eV.

In diverted discharge, the separatrix magnetic surface is located at

about 1.5 cm from the shell surface[3] and 30 % of the particle flux and
70-80 % of the heat flux diffused from the main plasma is guided into the
burial chamber. The scrape-off plasma parameters in the burial chamber
are; peak density in the vertical profile measured with a Langmuir probe
is 4×10^{12} cm^{-2}, peak electron temperature measured with a Faraday cup[4]
60-70 eV, ion temperature obtained by doppler broadenning 80 eV(CV) and
40 eV(CIV), and measured by the Faraday cup 60 eV. In non-diverted
discharge no particle and heat flux into the burial chamber are observed.

Particle confinement times obtained from ion saturation current to
the shells and the burial chamber wall is 2 ms in both discharges.

Fig. 3-4 shows the radial profiles of line radiation from the
intrinsic carbon ions at the current plateau. Solid lines indicate the
discharge with the divertor, and dotted lines without the divertor. These
Abel-inverted volume emissions of CVI (33.7 Å), CV (2270.9 Å), CIII (2296.9 Å)
are obtained by scanning the M.1 vertically and the non-circular effect is
neglected. The figure shows that, in the diverted discharge, the
intensity of lines from CIII is reduced 30 % and that from CV and CVI are
reduced by a factor of 2 than each intensity in the non-diverted one. The
intensity of line from CIII ions, which are much rapidly burnt than their
cross-field fiffusion time, represents the influx of carbon atoms at the
plasma outer edge. Therefore, it appears that a 30 % smaller impurity
influx at the plasma edge, the accumulation of higher ionized impurity
in the main plasma is reduced to half by the divertor action.

This situation is similar to the oxygen and metallic impurity present
in the discharge. In the diverted discharge, line intensities from oxygen
(OV (630 Å), OVI (1032 Å) and OVII (21.6 Å)) and metallic impurity (pseudo-
continuum emission in the range from 45 Å to 250 Å[5]) are reduced by a
factor of 2-3 than those in the non-diverted discharge.

The impurity injections are performed at 5-6 msec in the discharge by
the following manner. By using a fast acting gas value, 6.3×10^{17} molecules
of methane is injected with pulse duration of 1.5 msec through the gas inlet
placed at the farthest point from the divertor. A short burst of neutral
aluminum atoms with a velocity of 5×10^5cm/s is produced by irradiating a
0.2 μm thick aluminized glass slide with a 2.6 mm diam focased high-power
laser spot. The glass slide is located at 6 cm from the plasma outer edge.
An estimated $4\pm2\times10^{16}$ atoms are obliquely directed to the outer edge of
a scrape-off layer through a gap of shells.

The injected impurity atoms penetrate into the plasma before being
ionized. The ionization process continues as the ions rapidly move along
the field lines and, less rapidly, move across them. The transport of the
injected carbon ions towards the central region of the main plasma is
observed with M.1 and M.2, and that into the burial chamber is observed with
M.2.

3.2 Accumulation of the Injected Impurity in Discharges with and without Divertor

3.2.1 Methane Injection

With the methane injection for the diverted discharge, changes in
plasma resistivity and the total radiation loss measured by a pyro-
electric detector[5] are small and less than 15 %. The electron density
increase by 15 % and the electron temperature of main plasma column decrease
10 %. Since the changes in the plasma parameter are small, the increment of
the impurity accumulation with the injection is proportional to that of the
line intensity. This situation does not change in the non-diverted discharge
with the methane injection of same amount.

Fig. 3-5 shows the time development of the increments of line intensities
from CIII, CV and CVI in both discharges with methane injection of the same
amount. Solid lines indicate the discharge with the divertor and dotted lines
without the divertor. Fig. 3-5-a shows the injection phase : at 1 msec after
opening the gas valve. Almost same increment of CIII line emission in both
discharges indicates the same amount of additional carbon influx into the
plasma edge. This is consistent with the same amount of injected carbon
atoms. Fig. 3-5-b is at 2 msec. It shows the radial penetration phase of the
injected impurity toward the central region of the plasma. Increment of
the CV line emission for both discharges with and without divertor indicates
that the impurity influx into the main plasma column is reduced to half by
the divertor action. Fig. 3-5-c is at 4 msec when the radial penetration is
accomplished. CVI and CV line emission are reduced to half in the diverted
discharge. These observations make it clear that the radial impurity influx
toward the plasma center is reduced during the ionization process from CIII
to CV by the divertor action. This is apparently due to the shielding action
of the scrape-off plasma, and it is suggests that the half of the inward
carbon flux guided into the burial chamber as a ionization state of around

CIV.

At 4 msec in the Fig. 3-5, the peak value of the increased carbon ion in minor radius are; CIII$\sim$9×10^{10} cm^{-3}, CV$\sim$2×10^{11} cm^{-3}, which are calculated by using the modified coronal model for Be-like ions and He-like ions[6], and CVI$\sim$1.7×10^{11} cm^{-3}, which is calculated by using coronal model employing the excitation rate coefficient given in Ref.[7]. The ionization time τ_I of CVI in the central region is $\sim$0.3 msec[8]. Therefore, the injected carbon ions are dominantly in fully stripped state CVII at this time. Assuming that the n_e increase with the methane injection is due to stripping of 10 electrons from each of the injected methane molecules, 15 % increase of electron density of total number of 3.5×10^{18} results that total particles of accumulated carbon ions is 5.3×10^{16}. Using the CVI density obtained by spectroscopic measurement and CVII density deduced from the n_e increase, the confinement time τ of CVII ions in the central region can be estimated, and $\tau=\tau_I\times$CVII/CVI$\sim$3 msec. As the result of the injection of 6.3×10^{17} carbon atoms, 8-9 % of the injected carbon atoms is accumulated in the plasma. This also indicates that, in the non-diverted discharge, approximately 15-20 % of the injected carbon accumulate in the plasma. It appears that a shielding action against the injected impurity is present even in the non-diverted discharge.

A possible interpretation for this is that a large fraction of the injected particles are trapped on the surface of gas outlet, which is made of stainless steel, while they strongly interact with the surface during the injection phase. The rest carbon atoms spread along the field lines, diffuse across them and are recycling at the gold plated shell surface. During this process in the outer edge, a half of the ions are lost into the burial chamber in the diverted discharge.

3.2.2 Aluminum Injection

Since there is no intrinsic content of aluminum ions in DIVA discharge, the aluminum injection with sufficient line intensity from accumulated aluminum ions can be performed with no detectable change above $\sim$2 % in the plasma resistivity and electron density.

Fig. 3-6-a shows the time evolution of the line integral (across the minor diameter) of photon signals of AlXI (550 Å) with the aluminum injection of the same amount in discharges with and without divertor. Fig. 3-6-b shows the radial profiles of its volume emission at 3 msec after the

injection. Solid lines indicate the discharge with the divertor and dotted lines without the divertor. In both discharges, the signal starts to rise after 600-700 μsec from the laser irradiation, reaches the peak value at 3 msec and then decays with 3-4 msec time constant. Since AlXI 550 $\overset{o}{A}$ ($\Delta n=0$ transition) is insensitive to the electron temperature above 20 eV, the signal is proportional to $n_e \cdot N_{AlXI}$ where N_{AlXI} is the AlXI density. Therefore the increment of the intensity in Fig. 3-6-a indicates the radial penetration of injected aluminum ions towards the plasma center, and decay process indicates the ionization up to AlXII state or diffusive loss towards the wall. Different from the carbon injection case, the signal indicates no continued recycling of injected aluminum at the wall. As the result, for diverted discharge, the accumulation of the injected aluminum is reduced by factor of 3-4 than the non-diverted one.

The amount of maximum accumulation in minor radius deduced from the line intensity and the excitation rate coefficient give in Ref.[7] is 2.3×10^9 cm^{-3} for the diverted discharge. The ionization time τ_I of AlXI and AlXII in the central region of the plasma are 0.2 msec and 17 msec respectively, so that the dominant state is AlXII (He-like state). Since line emissivity from He-like state of aluminum ion is too weak to detect, the AlXII density is deduced by employing much more aluminum contamination with detectable n_e change ($\Delta n_e/n_e \sim 7$ %), and assuming that $n_e = 11 \cdot N_{AlXII}$. From this assumption and the spectroscopic measurement of AlXI density, we obtain that $N_{AlXII}/N_{AlXI}=22$ in the central region. By using this ratio, we estimate that roughly a 2×10^{15} aluminum ions accumulate in the diverted discharge. The confinement time τ of AlXII ions in the central region is; $\tau = \tau_I \cdot N_{AlXI} \sim 4-5$ msec. Thus for the injection of $4(\pm2)\times10^{16}$ aluminum atoms, with an uncertainty of a factor of 2-3, 5 % and 15-20 % of the injected aluminum atoms accumulate in the discharge with and without divertor respectively. These results are very similar to the case of carbon injection. The reason for the much more reduction of the impurity accumulation by the divertor action for the aluminum injection case is probably in the oblique injection and no-recycling at the wall.

3.3 Observation of Parallel Flow of Injected Impurity Along the Scrape-off Field Lines

By scanning the aluminum mirror horizontally in the diverted discharge with methane injection, the increase of line emissions from injected carbon

ions in the burial chamber and in the main plasma is observed. Fig. 3-7 shows the line integrated photon emissivity along the two paths indicated in the figure. The solid lines indicate the line emissivities from the intrinsic carbon content, and dotted lines that from the content with the injected carbon atoms. In the observations of main plasma, sudden increase of the CII-CIV line intensity indicates the spreading of the injected impurity ions in the outer edge of the main plasma. As was discussed in sub-section 3.2, the increase of CV line intensity mainly indicates the cross field diffusion of the injected carbons towards the hot main plasma.

The appearence of the increment of the light emission in the burial chamber is interesting. The increase of CII line emission is very little. Time behavior of the increase of CIII (2297 $\overset{\text{o}}{\text{A}}$) line emission is consistent with the wave form of the methane gas pulse of 1.5 msec duration. The largest increment can be found in CIV line emission. The increase of CV line emission is slower than of that in the main plasma.

Fig. 3-7 shows the delayed time of the flow-front of the injected carbons as CIII state at the divertor throat (R=46 cm). It shows that it takes 300±100 µsec for appearing in the burial chamber.

These observations in the burial chamber make clear the following .

1) No increment of CII line emission in the burial chamber indicate that the observed increment of CIII is not due to the ionization of the increased neutral carbon atoms in the burial chamber. That is, the injected carbons are successively ionized while their poloidal excursion in the scrape-off layer and a part of them appear as the CIII state in the burial chamber.

2) Although we have not made an absolute measurement of the various carbon ionized states in this observation, the signal suggests that the appearance of the injected carbons in the burial chamber are dominantly around the CIV state.

3) The increment of CV line emission in the burial chamber does not mainly show the direct flow of the injected carbons into the burial chamber along the scrape-off field lines, but the guidance of the diffusive loss flux of highly ionized ions from the main plasma through the scrape-off field lines into the burial chamber.

Now it appears that the appearance of injected impurity flow as CIII-CIV state in the burial chamber corresponds to the vertical observations presented in sub-section 3.2 that a half of the injected impurity influx

is disappeared during the successive ionization process from CIII to CV.

Adding to this shielding action by the divertor, it must be noted the following. As the result of the methane injection, the carbon content in the main plasma is nearly doubled. The loss flux of the carbon ions to the shell surface is also doubled as shown in Fig. 3-7. In the figure, CII and CIII line emissivities from the main plasma edge, which present the recycling flux at the gold plated shell surface, increase by a factor of 2. This can be recognized from the confinement property of carbon ions ($\tau \sim 3$ msec) discussed in sub-section 3-2. Similar to this impurity loss flux to the shell surface across the field lines, the increase of CV line intensity in the burial chamber presents the impurity loss flux as the highly ionization state into the burial chamber through the scrape-off field lines. That is, a part of the highly ionized impurity out-flux from the main plasma is swept out into the burial chamber.

3.4 Discussions and Conclusions

The transport of the injected carbon ions along the scrape-off field lines into the burial chamber is interesting. The electron impact ionization times of respective ionized state of carbon atoms[8] in the scrape-off plasma of electron density $\bar{n}_e \sim 2\times10^{12}$ and electron temperature ~ 60–70 eV are : 4 μsec, 20 μsec, 100 μsec, 400 μsec for CI, CII, CIII and CIV, respectively. The fact that the observed ionization states of the injected carbons in the burial chamber are around CIV state is consistent with the successive ionization process estimated from these ionization times in the scrape-off plasma parameter during the 300 ± 100 μsec of the poloidal excursion time. The injected carbon atoms are quickly ionized (~ 20–30 μsec) up to CIII state at the plasma edge before making remarkable poloidal excursion. At this ionization state by the collisional heat exchange between the ions ($Z_{eff} \sim 3$), the injected carbon ions are heated up to the bulk ion temperature (~ 40 eV) with the time constant of 60 μsec. The thermalized CIII or CIV ions make much collisions with the bulk ions before traveling into the burial chamber with the thermal velocity v_t : $\pi q R/v_t \tau$ $8 \sim 15$, where τ is the impurity-ion collision time. Therefore, the diffusion process along the scrape-off field lines is dominated by collisional effect. The diffusion time needed for the poloidal excursion is $(\pi R q)^2/\tau \cdot v_t^2 \sim 4 \sim 8$ msec, where $q(\sim 5)$ is the safety factor. This is too long compared with the experimental observation. This appears the existence of strong directional forces towards

the burial chamber. Since the collisional momentum transfer time in the scrape-off plasma is only 60 μsec, the injected carbon ions should be accellerated by the bulk scrape-off plasma flow.

Flow velocity of the bulk plasma along the scrape-off field lines in the burial chamber measured by a one-side probe[4] is 0.2-0.5 C_s, where C_s is the sound velocity. With this flow velocity, the transit time is $\pi Rq/0.3\ C_s \sim 190$ μsec. The observed transit time of the injected carbons is well explained with this velocity. Adding to this collisional process, the transport process of the impurity ions should be influenced by space potential along the scrape-off field lines. Impurity transport including above noted directional forces and atomic process in a scrape-off layer is under investigation by a numerical method and will be published elsewhere.

We have injected a pulse of methane gas and a short burst of aluminum into DIVA discharges with and without divertor. The results are summarized as follow:

1) For the methane injection and aluminum injection of same amount, the accumulation of the injected impurity ions in the main plasma is reduced by factor 2-4 by the divertor shielding action. Shielding efficiency is higher for aluminum than for carbon.

2) In the methane injection for the diverted discharge, the radial impurity flux towards the main plasma center is reduced during the successive ionization process from CIII to CV. It corresponds to the fact that the ionization state of the injected carbon ion flow into the burial chamber is around CIV. This presents the impurity shielding action of the divertor.

3) The impurity shielded in the scrape-off layer is rapidly guided into the burial chamber. The time needed for the poloidal excursion of the injected impurity in the scrape-off layer is equal to that of scrape-off plasma.

4) Impurity ion flux of highly ionized states into the burial chamber increases with the increase of the impurity content in the main plasma. This exhibit the sweeping action of the divertor, i.e. a part of the impurity ions diffused from the main plasma is swept out into the burial chamber through the scrape-off layer.

5) Shielding action is also very high even in a conventional tokamak.

6) Confinement time of carbon and aluminum are estimated to be 3∿5 ms.

This value is comparable to the average particle confinement time (2 ms).

References

1) Stott, P.E., Burt, J., Erents, S.K., et al., in Plasma Wall Interaction (Proc. Symp. 1976) Pergamon Press (1977) 39.

2) SHIMOMURA, Y., et al., Phys. Fluids 19 (1976) 1635.

3) Yamamoto , S., Sengoku, S., Kimura, H., et al., "Behaviour of Super-thermal Electrons in the Scrape-off Layer of DIVA", to be published in Nucl. Fusion.

4) Kimura, H., Nagami, M., Yamamoto , S., et al., Japan Atomic Energy Research Institute Report JAERI-M 6971.

5) Shiho, M., Odajima, K., Sugie, T., et al., Japan Atomic Energy Research Institute Report JAERI-M 7432 (1977).

6) Gabriel, A.H., Jordan, C., "Case Studies in Atomic Collision Physics II, Chapter 4" North-Holland (1972).

7) Mewe, R., Astron. and Astrophys. 20 (1972) 215.

8) Lotz, W., Zeitschrift für Physik 216 (1968) 241.
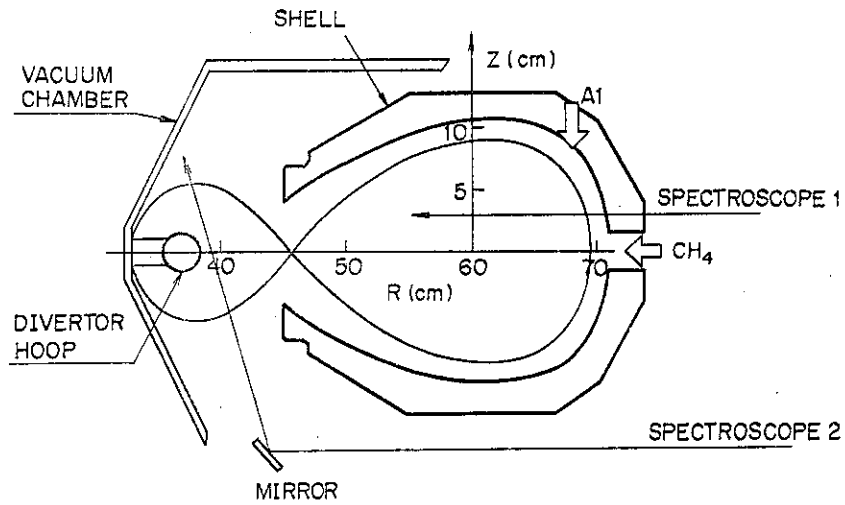
Fig. 3-1 Cross sectional view of DIVA tokamak and experimental
          arrangement showing the position of methane and aluminum
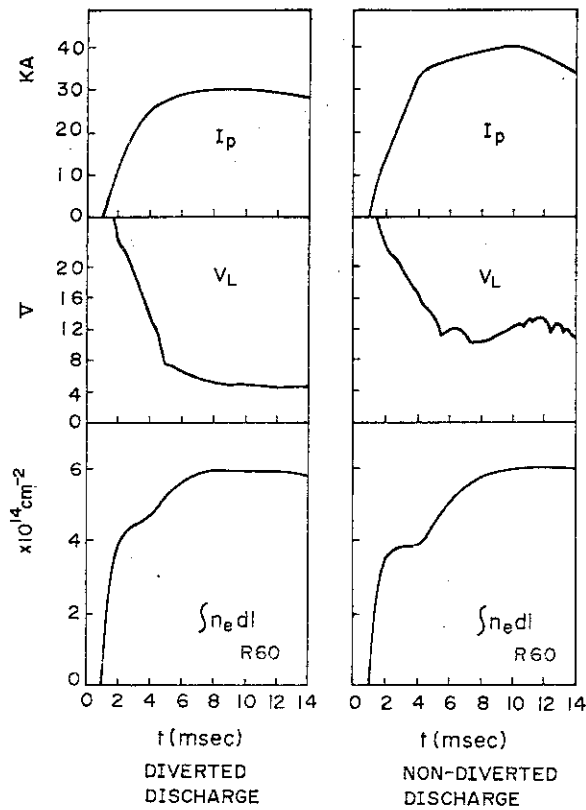   injection, and sight-path of three monochromators.

Fig. 3-2 The time development of plasma current I_p, plasma loop voltage
          V_L, and the line integrated electron density $\int n_e d\ell$ at R=60 cm
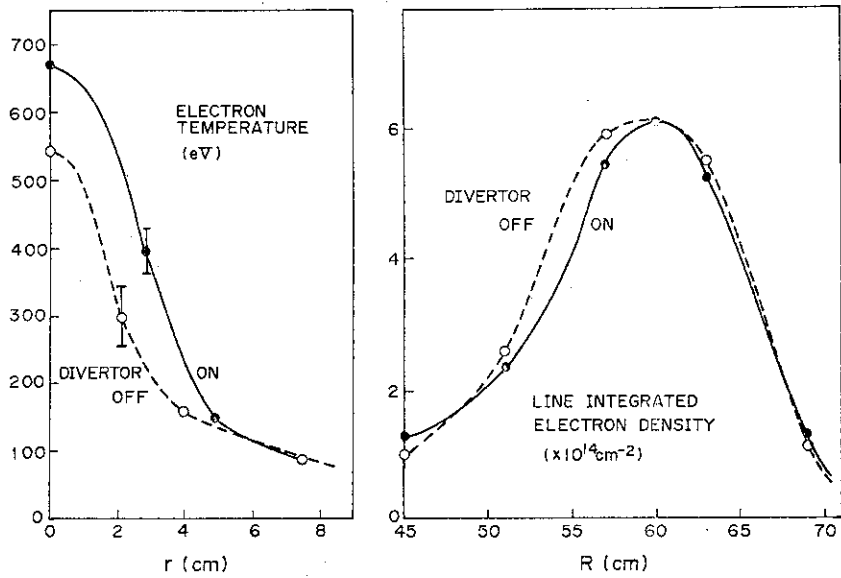   for discharges with and without the divertor.

Fig. 3-3   The electron temperature profiles in minor radius and line
integrated electron density profiles in major radius in
discharges with (solid lines) and without (dotted lines) the
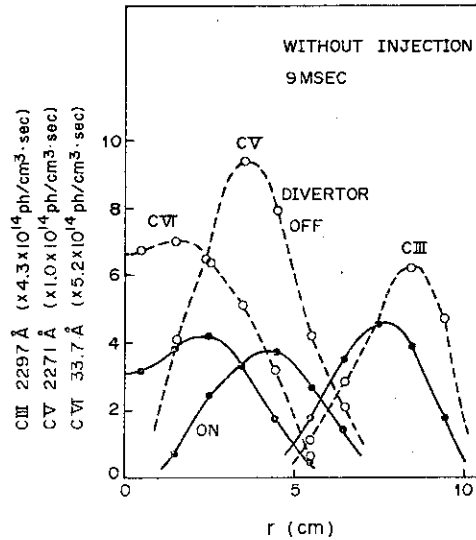divertor at the current plateau.

Fig. 3-4   Comparison of line emissivities from the respective ionization
states of intrinsic carbon ions in discharges with and
without divertor.   Similarly in the diverted discharge, line
intensities from oxygen (OV 630 Å, OVI 1032 Å, OVII 216 Å) and
metallic impurity (pseudo-continuum) are reduced by factor
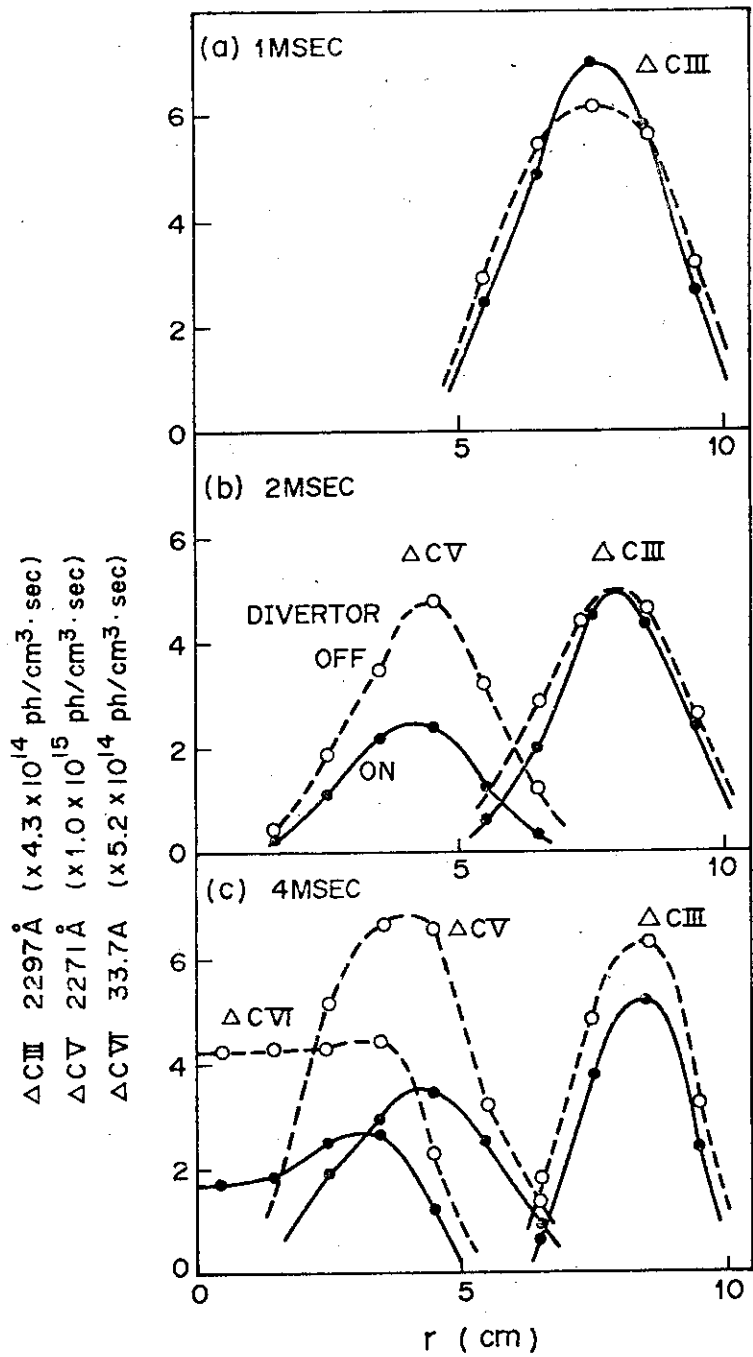2-3 than the non-diverted one.

Fig. 3-5 Time development in the increments of CIII (2297 Å), CV
(2271 Å) and CVI (33.7 Å) after the start of the methane
injection; a) during the injection phase, b) radial
penetration phase, c) the penetration is accomplished.
The accumulation of the injected carbon ions in the main
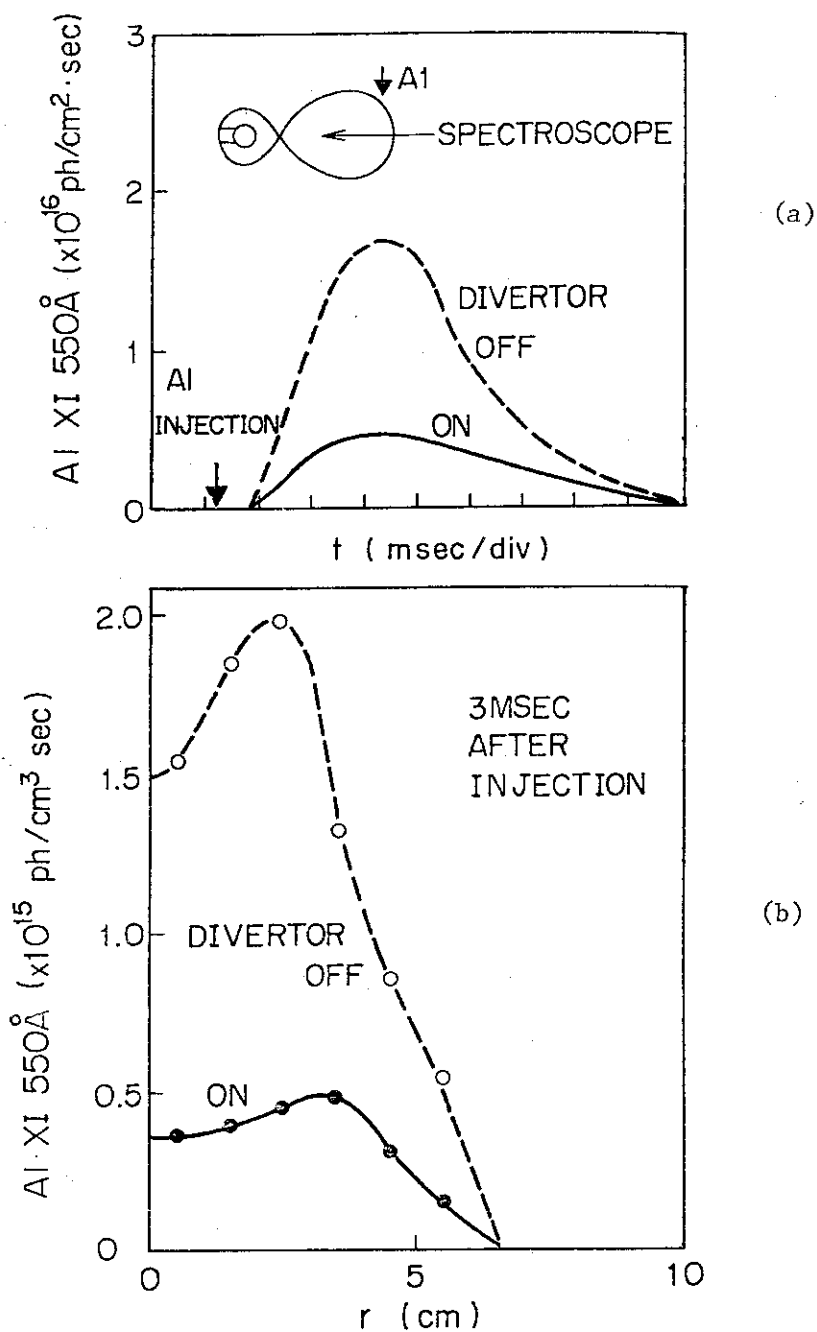plasma is reduced to half by the divertor action.

Fig. 3-6 a) Time development of the line integrated emissivity of
AlXI 550 A with the aluminum injection. b) Abel-inverted
volume emission of AlXI 550 A after 3 msec from the injection.
Accumulation of the injected aluminum ions in the central
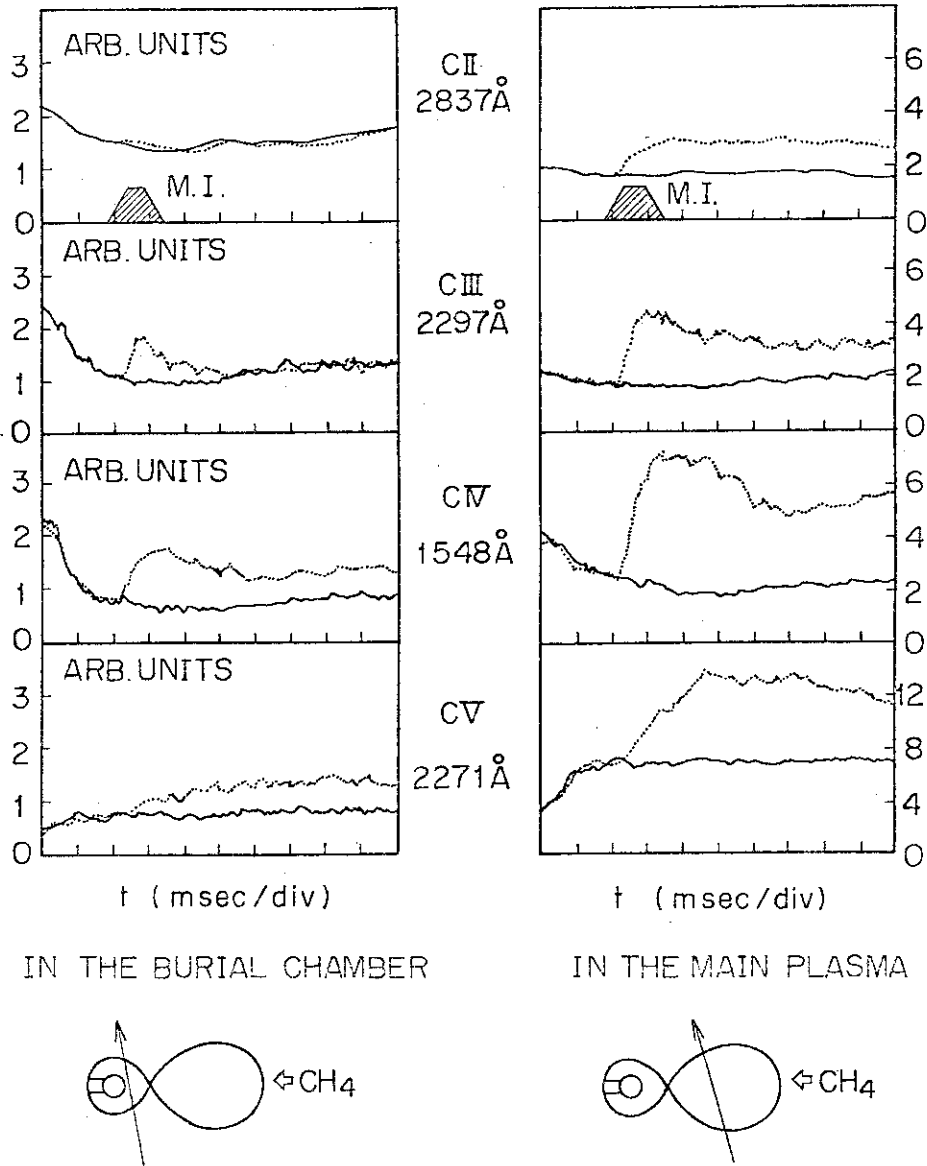region of the plasma is reduced by factor 3-4 by the divertor
action.

Fig. 3-7   Time divelopment of the increase of line intensity from
respective ionization states of carbon ions in the burial
chamber and in the main plasma with the methane injection
(M.I.) in diverted discharge.   ——: without injection,
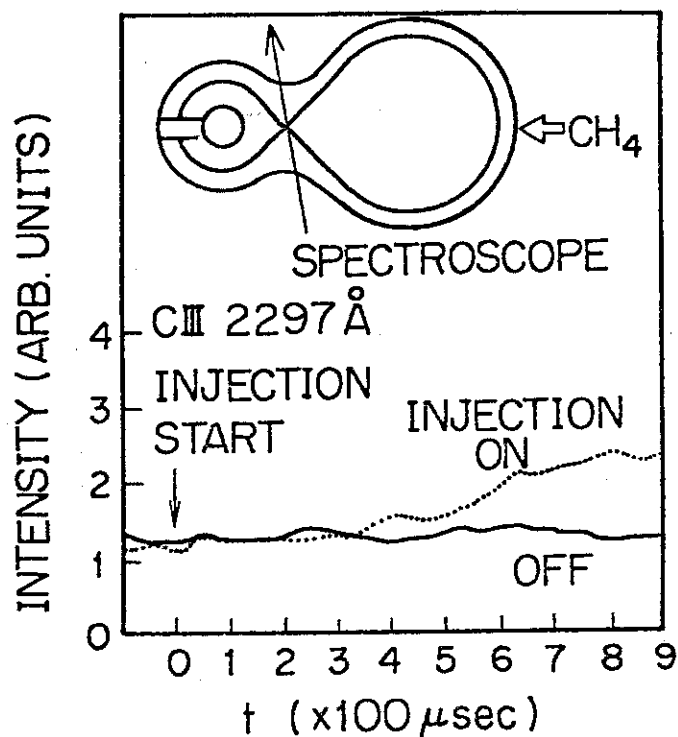........: with injection.

Fig. 3-8 The increase of CIII (2297 Å) line emission in the burial chamber with the methane injection. The delayed time of the increment from the start of the injection presents the time needed for the poloidal excursion of the injected carbon ions along the scrape-off field lines.

4. Spectroscopic Study on Low-z and High-z Impurities

Many investigations on impurities have been done in various tokamaks.[1]-[4] Recently, closely crowded many lines from heavy ions were observed and were shown to emit a significant fraction of input power in DIVA[5] and ORMAK[6]. The radiation loss due to heavy impurities becomes much more serious in a future large tokamak because these impurities are only partially ionized even in a reactor plasma. Identification of these many lines was tried in ref.(6) and absolute radiation power was measured in a low-z free plasma[5] but no detailed study has been done. Spectroscopic study on heavy impurities as well as light impurities are described in this section. Power spectrum and radial profiles of the closely crowded many lines are studied. Concerning the light impurities, density profiles and profiles of radiation power are studied. The major results are following: Oxygen is the dominant impurity in light impurities and its content is 2%. The pseudo continuum is observed in a range of 45 - 200 $\overset{o}{A}$ and has internal structure, i.e. the radial intensity profile has a peaked profile at a short wavelength and a hollow profile at a long wavelength. The radiation loss power is 30 kW from oxygen and carbon and 25 kW from heavy impurities.

In the next subsection we discribe the plasma parameters and the experimental set-up. In 4.2 light impurities such as oxygen and carbon ions are studied and in section 4.3 closely crowded many lines in the range of 45 to 200 $\overset{o}{A}$ in detail. Discussions and conclusions are given in 4.4.

4.1 Experimental Set-Up and Plasma Parameters

In order to obtain the spatial distribution for impurity emission, the vacuum monochromator is set up on a vertically scanning port as shown in Fig. 4-1. In the present study all measurements were done with the spatial resolution of 1 cm in the plasma region, which is obtained by inserting several diaphgrams between the plasma and the monochromator.

A 3m grazing-incidence monochromator used in measurements is equipped with a 600 grooves/mm and 1200 grooves/mm gratings, which are exchangable each other and coated with platinum. The monochromator is calibrated absolutely by means of the atomic branching-ratio method using suitable line-pairs, i.e. CV (40.73 $\overset{o}{A}$, 2277.92 $\overset{o}{A}$), OVI (150.1 $\overset{o}{A}$, 3811.35 $\overset{o}{A}$), OIV (238.5 $\overset{o}{A}$, 3411.76 $\overset{o}{A}$), CIV (312.43 $\overset{o}{A}$, 5801.51 $\overset{o}{A}$), OIII (320.98 $\overset{o}{A}$, 3961.59 $\overset{o}{A}$),

OII (515.5 Å - 4943.06 Å) and H (1025.72 Å, 6562.8 Å), from the plasmas in DIVA (JFT-2a) and JFT-2.

Figure 4-2 shows time-variations of various plasma parameters in the discharge in which the ratio of divertor current I_D to plasma current I_p is 1.2. The peak plasma current is 40 kA and the loop voltage V_L is 4 V. Peak electron and proton temperatures at the plasma center are 700 eV and 270 eV, respectively. The peak electron density is 8×10^{13} cm^{-3} at the plasma center. Under this discharge condition, time- and space-variations of intensities of oxygen and carbon lines and closely crowded many lines were measured by scanning a 3m grazing-incidence vacuum monochromator. (We shall hereafter call crowded many lines as pseudo-continuum).

4.2 Light Impurities

The time-evolution of radiance in photons/cm$^2 \cdot$sr$\cdot$sec for emission from oxygen ions (OV-OVIII) and carbon ions (CV and CVI) are shown in Fig. 4-3. In the figure, the radiance of emission lines from light impurity ions is found to be approximately stationary near at 10 msec, and the plasma parameters, i.e., electron temperature and density, revealed quasi-stationary variation as shown in Fig. 4-2. At this time, radial density profiles of these ions are investigated and Fig. 4-4 shows radial profiles of the population density for oxygen (OV, OVI, OVII and OVIII) and carbon (CVI) ions in the ground-state. Profiles of the electron temperature and density are also shown in the same figure. In the DIVA plasma with the central electron temperature T_{eo}=700 eV, the OVIII ion with the ionization potential of 871 eV has a peaked profile and the other ions have a hollow profile. The population density of OVIII and OVII ions is an order of 10^{12} cm^{-3}, and for lower ionized oxygen ions, i.e., OVI and OV, the density is less than that of more highly ionized ones by an order of 2 or 3. Integrating the density over a minor radius r, content of the oxygen impurity is obtained to be 2% of the total electron amount. On the other hand carbon impurity is less than one percent of the total electron amount. In the above estimation, we consider fully stripped ions such as OIX and CVII. The densities of fully ionized ions are calculated by employing a corona-model involving a particle diffusion term. This term is calculated from the profiles of oxygen ions in Fig. 4-4. These results for the density of oxygen and carbon ions give

the effective ionic charge Z_{eff} at the plasma center to be 2-3.

Radiation power by line emission from oxygen and carbon ions is obtained from the measured intensity for these lines and calculated values for the second and third resonance lines assuming a coronal equilibrium. Solid curves in Fig. 4-5 indicate radial profiles of radiation power from OVIII, OVII, OVI and OV ions. The values shown in this figure are obtained by multiplying the density of radiation power by $4\pi^2 rR$, where r and R are minor radius and major radius, respectively. The total radiation power by oxygen ions is approximately 25 kW and that by carbon ions is less than about (5-10) kW.

4.3 Heavy Impurities

Intense emission is observed in the range of 45 - 200 Å and is considered to be originated mainly from gold ions as described in 2.4. Figure 4-6 shows the distribution of radiation power in watt/cm²·sr·Å of the pseudo-continuum integrated along the line of sight at 10 msec. This radiation power is obtained after subtructing a light in the second and third orders and a stray light. Figure 7 shows profiles of radiation power density of the continuum at 60, 98, 150 and 175 Å. The profiles have a peaked profile at 60 Å and 98 Å and a hollow profile at 150 Å and 175 Å. This result indicates that the pseudo-continuum distributed in the range of 45 to 200 Å has a sparial internal-structure. Radiation from the pseudo-continuum below 110Å concentrates in the central region of the plasma with T_{eo}=700 eV and that above 110 Å has a peak value in the intermidiate region between central and peripheral regions or $T_e \approx 200$ eV. The difference of these profiles by wavelength or energy suggests that the pseudo-continuum below 110 Å are ascribed to emission from heavy ions with more multiply ionized states than those of the ions emitting radiation in the range of 110 to 200 Å. In order to estimate radiation power of the pseudo-continuum, we assume that the profile of the pseudo-continuum above 110 Å has the same profile as that at 150 Å and 175 Å, and that below 110 Å has the same profile as that at 60 Å and 98 Å. The profile of radiation power due to the pseudo continuum is shown in Fig. 4-5 and the total radiation power is 25 kW.

4.4 Discussions and Conclusions

Impurity radiations are investigated in a range of 10 - 1300 $\overset{\circ}{A}$ by vertically scanning a calibrated 3m grazing-incidence monochromator. Oxygen is the dominant impurity in light elements and its content is 2 % of electron density. Radiation power by light impurities is 30 kW. Intense emission due to heavy impurities is observed in a range of 45 - 200 $\overset{\circ}{A}$. This result is contrast with the previous experiment in which the pseudo continuum was observed in a range of 120 - 250 $\overset{\circ}{A}$ with a lower electron temperature, i.e. about 250 eV (see Appendix II). This pseudo continuum has internal structure, i.e. the intensity of the radiation at the short wavelength ($\underset{\sim}{<}$ 100 $\overset{\circ}{A}$) has the maximum value at the plasma center with T_{eo}=700 eV and that at the longer wavelength ($\underset{\sim}{>}$ 100 $\overset{\circ}{A}$) has the maximum value at r=4 - 5 cm or $T_e \approx 200$ eV. These results suggest that emission at the short wavelength comes from more highly ionized ions and that at the longer wavelength from ions with lower ionization-states. Unfortunately, spectrums from heavy elements are not clarified. The content, however, can be roughly estimated from the measured radiation power assuming the radiation power from gold calculated by D.E. Post et. al. The estimated content is about 0.05 %. The measured radiation power due to the pseudo continuum is 25 kW. The total radiation loss power due to heavy and light impurities is 55 kW but the total radiation measured by a pyroelectric detector is 30 kW as described in Sect. 2. The difference has not been understood but may be due to the errors of these measurements. The effective ionic charge is estimated 2-3 which comes mainly from oxygen and is consistent with the value estimated from the plasma resistivity.

References

1) Hinnov, H., Phys. Rev. A14 (1976) 1533.

2) TFR Group, Phys. Rev. Letters 36 (1976) 1306.

3) Bretz, N., Dimock, et al., Nucl. Fusion 15 (1975) 313.

4) Equipe TFR, Nucl. Fusion 15 (1975) 1053.

5) Maeda, H., et. al., in Proceedings of the International Symposium on Plasma Wall Interaction, Jülich, 1976, (Pergamon Press, 1977), P.537.

6) Colchin, R.J., et. al., ibid, P.95.

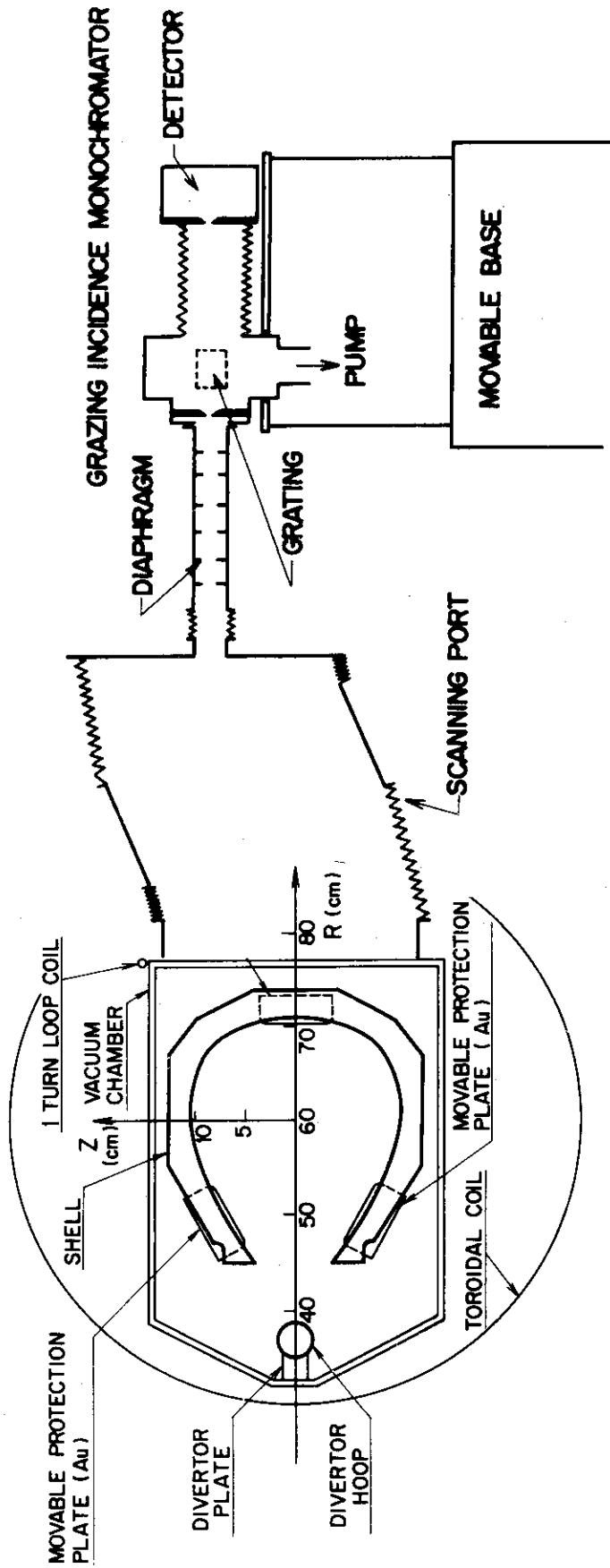7) Post, D.E., et. al., Princeton Plasma Physics Laboratory Report PPPL-1352 (1977).

Fig. 4-1 Cross-sectional view of the DIVA device and a 3m grazing-incidence vacuum monochromator.
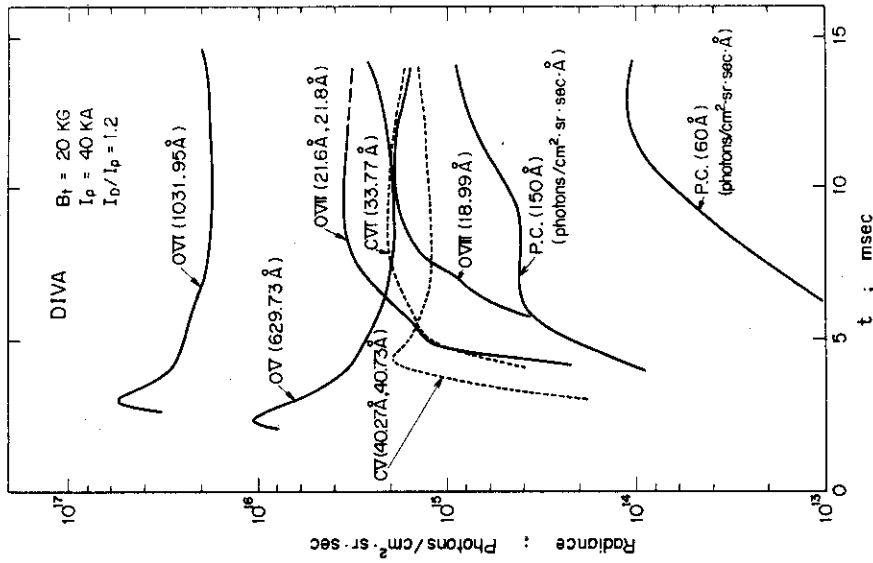
Fig. 4-3 Time-evolutions of radiance for emission from light impurity ions and for the pseudo-continuum emission (P.C.) at 150 and 60 Å in photons/cm²·sr·sec·A.
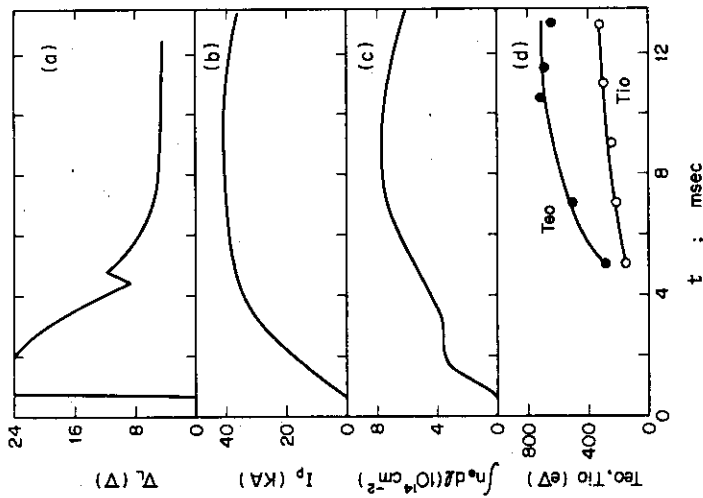

Fig. 4-2 Time-variation of plasma parameters of the DIVA plasma with $B_T=2$ T, $I_D/I_p=1.2$.: (a) loop voltage V_L, (b) plasma current I_p, (c) integrated electron density along the central chord, (d) central electron temperature T_{eo} and central proton temperature T_{io}.
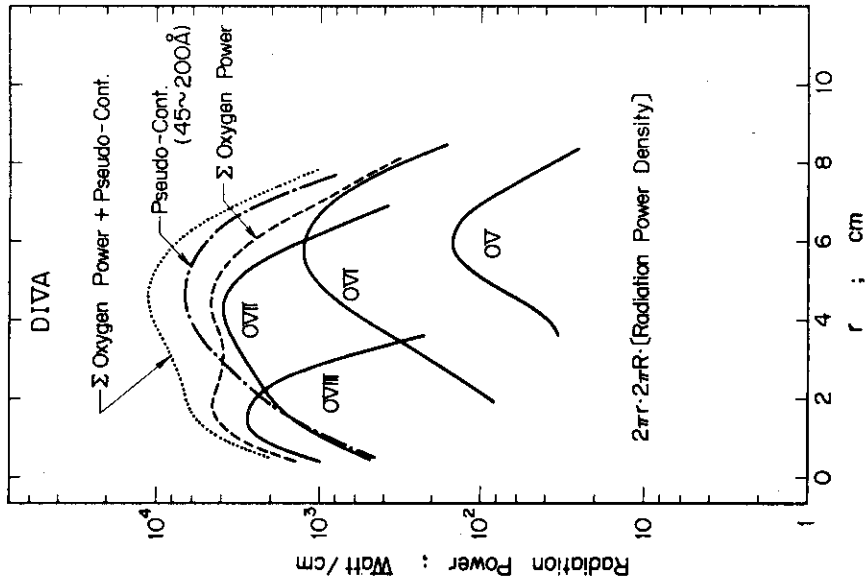
Fig. 4-5 Radial profiles of radiation power in watt/cm for oxygen ions and the pseudo-continuum in the range of 45 to 200 Å. Broken curve is the distribution of radiation power from oxygen ions, and doted curve is the distribution of total power from oxygen and pseudo-continum.
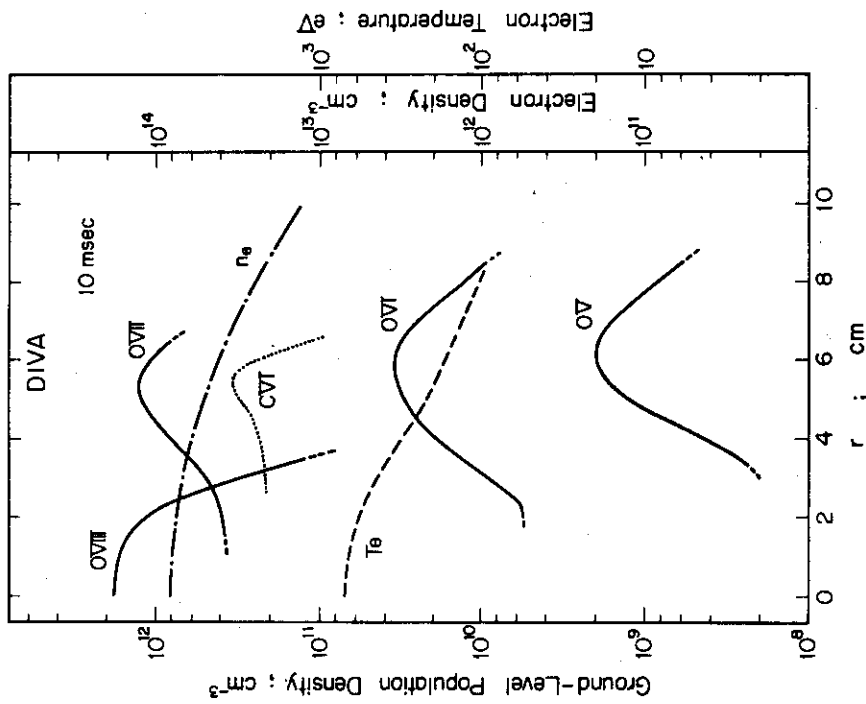

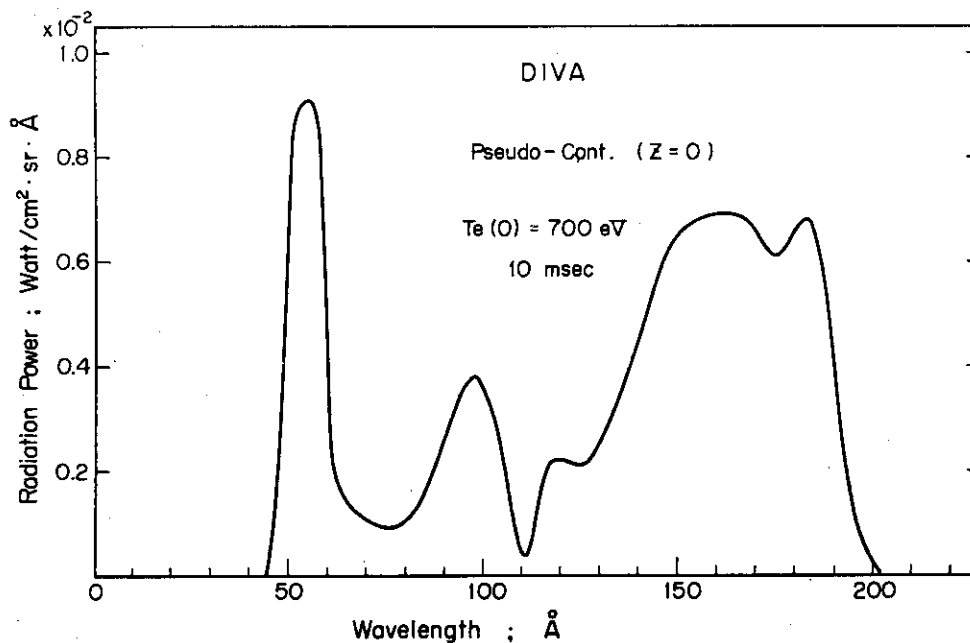Fig. 4-4 Radial profiles of the population density for OV, OVI, OVII, OVIII and CVI ions.

Fig. 4-6 Wavelength dependence of the pseudo-
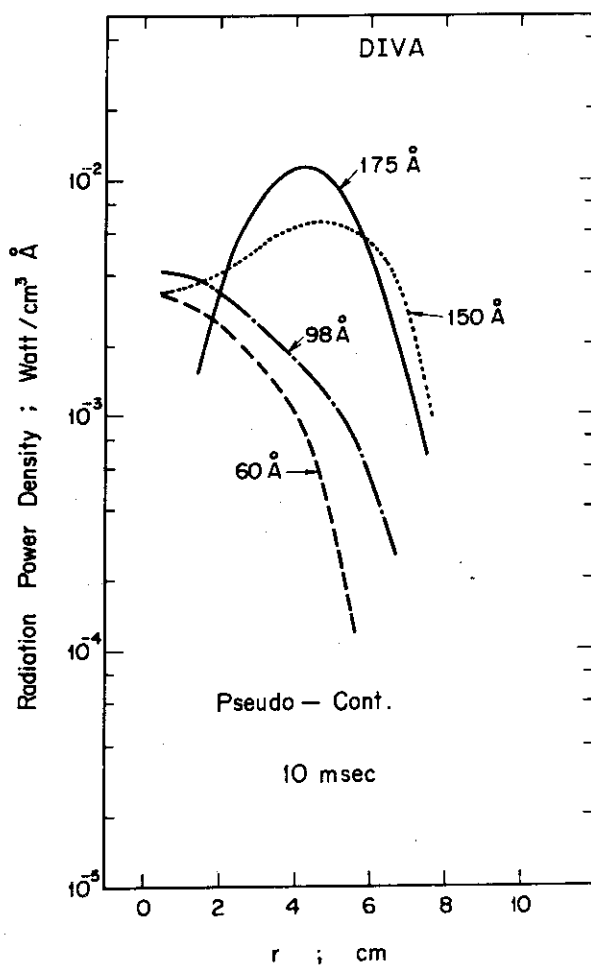continuum indicated by radiation power
at 10 msec.

Fig. 4-7 The profile of radiation power density
for the pseudo-continuum at 60, 98,
150 and 175 A.

5. Origin of Metal Impurities

It is well known that the impurity contamination into the plasma causes an increase in the radiation losses and a decrease of the energy confinement time.[1] Moreover it also causes a decrease of the deuteron and toriton density. This means that the efficiency of nuclear fusion decreases. Therefore the reduction of the impurity contamination is one of the important problem to be solved to realize the thermonuclear fusion project. Many efforts to reduce the light impurities, such as oxygen and carbon, have been done and it has been found that if the first wall surface was made clean by the method of, for example, the flash of titanium, the light impurity contamination could be reduced.[2] However as the light impurity contamination is reduced, the metal impurity contamination increased and the radiation loss due to the metal impurity consumes the main part of the ohmic input power.[3] Therefore the research of the mechanism of the metal impurity release, its contamination in the plasma and the method of the reduction of the metal impurity influx and contamination become more important. J.L. Craston et al. pointed out that the unipolar arcing is the dominant process of the release of the metal impurity in ZETA.[4] However there is few works concerning to this problem about the light impurity free tokamak plasma. It must be pointed out that arcing occurs easily if the condition of reoxidation of the surface is satisfied.[5] In this section the origin of the metal impurity from the surface contacts to the scrape-off plasma, that is limiter, is described. The three processes of the release of the metal impurity, that is ion sputtering, evaporation and arcing, are identified and shown to occur under the different condition of the limiter surface and the potential drop with respect to the plasma. Among these processes, it is made clear that the ion sputtering is the dominant process of the release of the metal impurity from the limiter for the stationary tokamak plasma.

In the following sub-section, experimental arrangement is described. Experimental results are given in 5.2 and discussions in 5.3.

5.1 Experimental Procedure

The experimental arrangements are shown in Fig. 5-1. The plasma in the divertor region of DIVA[6] is used to simulate the scrape-off plasma of the conventional tokamak. The parameters of the divertor plasma are as

follows; T_e=50-60 eV, T_i=60-80 eV and n_e=2×10^{12} cm^{-3}. An Al target of 6 cm^2 in area located normal to the magnetic field in the divertor simulates the toroidal limiter in the conventional tokamak. The length of the corresponding toroidal limiter is a quarter part of the torus. Aluminium was chosen as the metal impurity because it is not used elsewhere in DIVA and it is clear to decide the position of the impurity source of aluminium. This target is positively or negatively biased with respect to the plasma. At the time when the plasma reaches its stationary state (about 8 ms after the beginning of the discharge), electrical bias is added to the Al target. The time duration of the pulse is 2 ms and this pulse does not cause any change in the macroscopic discharge characteristics such as the plasma current, loop voltage, plasma density and electron temperature. The voltage of the pulse added between the Al target and the vacuum vessel is changed shot by shot. The probe characteristics of the target, the time evolution of the target current and the time variation of the intensity of Al-III line radiation (3602 Å) are measured. The monochromator is arranged to view directly the target.

5.2 Experimental Results

The results are shown in Fig. 5-2 and Fig. 5-3. Fig. 5-2 shows three different type of the time evolution of the intensity of Al-III line radiation and the target current. In Fig. 5-3 the intensity of the line radiation and the target current are plotted as a function of the applied voltage to the target respect to the vacuum vessel. The floating potential of the target is zero volt in this figure. From these experimental results, the three different types of the origin of the metal impurity release from the limiter into the plasma are identified as follows.

(1) ION SPUTTERING

As shown in Fig. 5-3, when the applied voltage to the target is negatively increased, the intensity of the Al-III line radiation continues to increase, whereas the target current saturates at 6 A, that is the level of the ion saturation current. The fact that the target current saturates means the ion flux to the target is constant. But the energy of the colliding ions to the target is increased as increasing the applied voltage. The dependence of the amount of the impurity influx on the energy of the colliding ion indicates that in this case the impurity release from the

target is caused by ion sputtering. The typical time evolution of the intensity of the Al-III line radiation and the target current correspond to the dotted points in Fig. 5-3 are shown in Fig. 5-3-a. The time delay in the change of the Al-III line radiation is relatively short as shown and within 200 μs, that corresponds to the characteristics time of the ionization and the excitation of the aluminium to the state of this radiation in the divertor plasma. The short time delay of the release of the aluminium from the target and the time independent impurity influx into the plasma also indicates that the mechanism of the release is not the thermal process but the atomic process, i.e. ion sputtering. Moreover, as shown by the solid line in Fig. 5-2-c, when the floated target is biased positively to retard the ion, the intensity of the line radiation of aluminium is decreased to the level without the target if the pulse duration is short and the heat flux is small enough.

(2) ARCING

As shown in Fig. 5-3 by the crossed points, the large target current is observed. The time evolution of the target current and the intensity of Al-III line radiation is shown in Fig. 5-2-b. This class of the release of the metal impurity is orbiously distinguished from the class of ion sputtering described above. As shown in Fig.5-3, the target current is 40 A, that is larger than the ion saturation current by the factor of ten, and increased as the applied voltage increased. The larger target current indicates that the mechanism of the release of the metal impurity for this class is arcing as pointed by R. Hancox et al.. The arcing is observed only in the first about ten shots after inserting the target into the divertor plasma. This indicates the conditioning effects widely observed in discharge phenomena and also suggests that the process of this type of impurity release corresponds to arcing.

(3) EVAPORATION

As shown in Fig. 5-2-c, when the target is positively biased and collects electron currents, the intensity of the Al line radiation is increased with the time delay of 1-2 ms. The electron current is greater than the ion saturation current by the factor of ten. In this case the heat flux to the target is greater than the case with positive biase. The time delay of 1-2 ms of the impurity release corresponds to the characteristic time of the aluminium target to melt. These results suggest that the mechanism of the release of the metal impurity in this class is

evaporation due to the heat flux by the electron.

5.3 Discussions and Conclusions

The processes described in the previous sub-section, occur under the different electrical and surface conditions of the target. The target in this experiment simulates the limiter in tokamak discharges.

The limiter is sometimes used as grounded or as floated electrically in conventional tokamka. Arcing occurs only when the limiter has negative potential to the scrape-off plasma, but can be easily suppressed by discharge cleaning of the limiter surface as shown in the present experiments. Arcing, however, may occur when the negative spikes appear. Evaporation may occur when the heat flux to the limiter is increased to the level about ten times greater than the normal heat flux by the stationary plasma. Although these processes may occur under the special condition of the plasma and the limiter surface, they do not occur when the plasma becomes its stationary state. The experimental results described above indicate that the ion sputtering is the dominant process of the release of the metal impurity from the limiter contacting to the quasi-stationary scrape-off plasma in tokamak.

In Fig. 5-4 the intensity of the line radiation, that correlates to the quantity of the metal impurity efflux by ion sputtering, is plotted as a function of the applied voltage to the target. The intensity of Al-III line radiation, and the Au-I line radiation when the shell coated by gold is biased, are also plotted in the same manner. These results suggest that when the accelerating potential is below 400 V, the main part of the ion sputtering may be caused by the impurity ions and above 400 V, the ion sputtering by the hydrogen may become dominant, because the energy gained by the ion of charge Z is Z-times greater than the energy gained by the hydrogen.[7] The results show that the high-Z impurity ion sputtering must be dominant when the sheath potential is as low as in the usual scrape-off plasma, i.e. $\phi \approx 150 \sim 200$ V. The contribution of the sputtering by the neutral atoms to the metal impurity contamination is concluded to be very little because of the electrical potential dependence on the metal impurity release. It is also demonstrated that the target of honeycomb structure can reduce the metal impurity influx by the factor of two. This experimental result supports the conclusion that the dominant process of the metal impurity release into the plasma is ion sputtering.

This conclusion shows that it is important to decrease the energy of the ion that sputters to the limiter or to reduce impurity influx into the main plasma in order to reduce the metal impurity contamination in the present tokamak plasma. The energy of the sputtering ion accelarated by the sheath potential can be decreased if the plasma temperature of the scrape-off layer is decreased. Therefore the control of the scrape-off plasma is the important techniques to avoid the metal impurity contamination.[8]

The divertor decreases impurity influx into the main plasma because the impurity source is removed far from the main plasma.

References

1) Jensen, R.V., Post, D.E., Jassby, D.L., Critical Impurity Concentration for Power Multiplication in Beam-Heated Toroidal Fusion Reactors, PPPL-1350 (1977); Breton, C., et. al., Nucl. Fusion 16 (1976) 891; Tazima, T., et. al., Nucl. Fusion 17 (1977) 419.

2) Stott, P.E., Daughney, C.C., Ellis, R.A., Nucl. Fusion 15 (1975) 431.

3) Berry, L.A., et. al., 6th Conf. on Plasma Phys. and Controlled Nuclear Fusion, Berchtesgarden (1976) Paper IAEA-CN-35/A4-1; Meservey, E.B., et. al., Nucl. Fusion 16 (1976) 593.

4) Craston, J.L., et. al., Proceedings of 2nd U.N. Conf. on Peaceful Uses of Atomic Energy, Geneve (1958) 414.

5) Hancox, R., British Journal of Applied Physics 11 (1960) 468; Guile, A.E., Proc. IEE, IEE Reviews 118 (1971) 1131.

6) Yamamoto, S., et. al., 8th European Conf. on Controlled Fusion and Plasma Physics, Prague, vol.I (1977) 33.

7) Kenknight, C.E., Wehner, G.K., J. Appl. Phys. 35 (1964) 322; Furr, A.K., Finfgeld, C.R., J. Appl. Phys. 41 (1970) 1739; Hayward, W.H., Wolter, A.R., J. Appl. Phys. 4C (1969) 2911; Almen, O., Bruce, G., Nucl. Instr. & Meth. 11 (1961) 279.
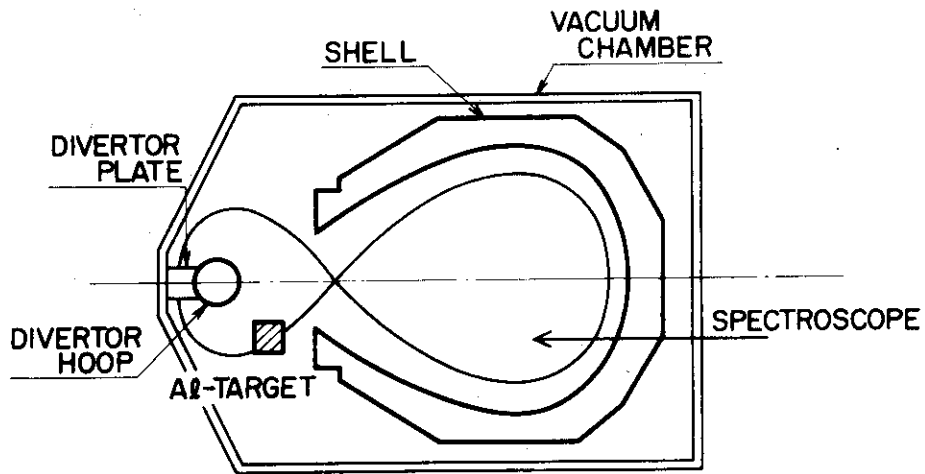
8) Shimomura, Y., Nucl. Fusion 17 (1977) 626.
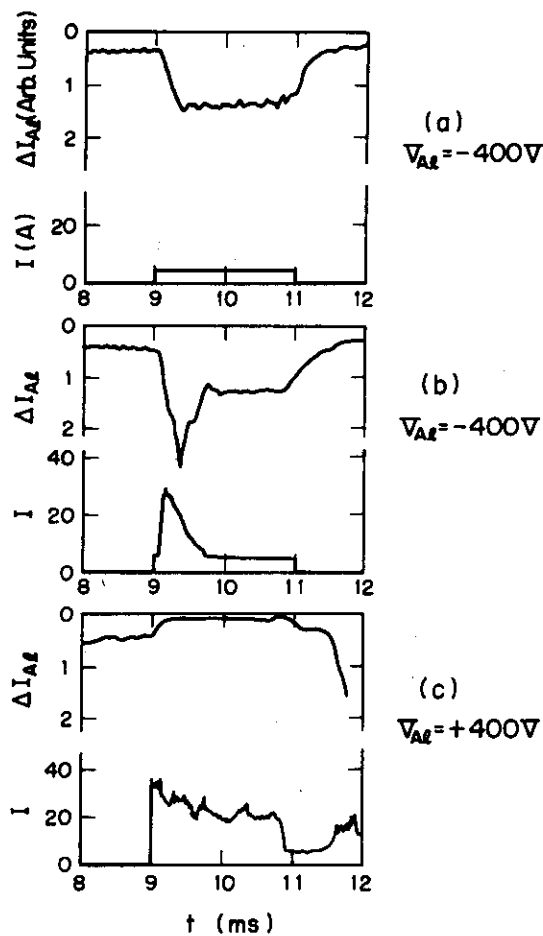
Fig. 5-1   Schematic of the experimental setup.

Fig. 5-2   Typical time evolutions of the intensity of Al-III line
radiation (3602Å) and the probe current.   The target is
biased from 9ms to 11ms.   The applied voltage of the pulse
is shown.   Each graph shows (a) Ion Sputtering, (b) Arcing,
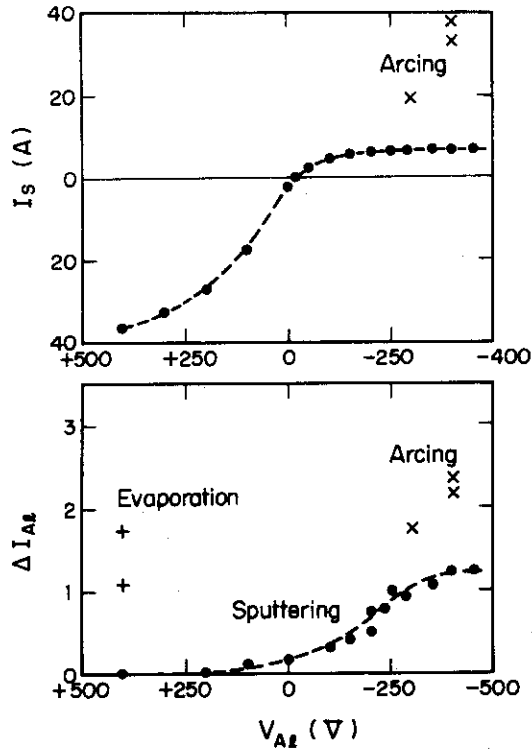(c) Evaporation, respectively.

Fig. 5-3 The dependence of the probe current and the intensity of the
Al-III line radiation on the applied voltage to the Al-target.
The experimental results are classed clearly into the three
types. Closed circles correspond to the type (a) in
Fig. 5-2-b, i.e. Ion Sputtering. Crossed points correspond
to the type (b) in Fig. 5-2, i.e. Arcing. Dagger points
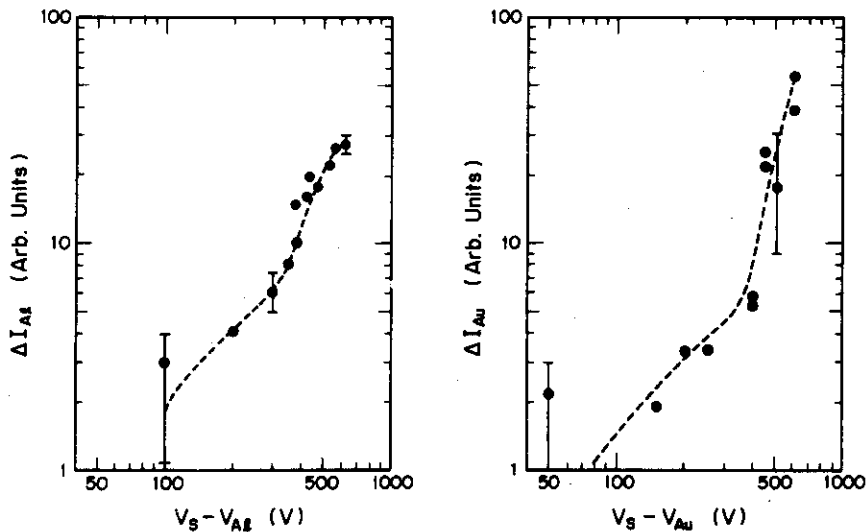correspond to the type (c) in Fig. 5-2, i.e. Evaporation.

Fig. 5-4 Dependence of the intensity of Al-III and Au-I line radiation
in the case of (a) in Fig. 5-2 on the applied voltage to the
Altarget or the gold plated shell. V_S-V_{Al} means the potential
gap between the plasma space potential and the Al-target.
V_S-V_{Au} means the potential gap between the plasma space
potential and the gold plated shell.

6. Summary

After increasing the maximum toroidal magnetic field from 1 T to 2 T, discharges have been obtained over a rather wide range of plasma parameters, i.e. electron temperature T_{eo}=200-700 eV, ion temperature T_{io}=60-300 eV and density n_{eo}=(1.5-8.0)×10^{13} cm^{-3} in the main plasma and T_{es}=20-100 eV, T_{is}= 20-60 eV and n_{es}=(1.5-5.0)×10^{12} cm^{-3} in the scrape-off layer plasma. With these parameters, the following investigations have been done and the results are summarized as follows:

(1) Divertor effects on impurities and radiation loss

The divertor reduces radiation loss due to both low- and high-z impurities by a factor of 2-4 by reducing plasma wall interactions (see (2)) and shielding impurity influx (see (3)). The reduction of the radiation loss by the divertor is more effective in a high current discharge because the divertor efficiency is high in a high current discharge. Impurity contents are also reduced by the divertor.

(2) Divertor efficiency for particle and heat

The maximum divertor efficiency is 35 % for particle flux and 75 % for heat flux. The efficiencies increase as increasing plasma current because the diffusion coefficient has the Bohm type coefficiency in the scrape-off layer plasma.

(3) Shielding action

The scrape-off layer plasma ionizes injected impurities and guides the ionized impurities into the divertor chamber. Consequently, influx of the injected impurities into the main plasma is reduced by a factor of 2-4 by the divertor. The travelling time of the injected impurities to the burial chamber is equal to that of the scrape-off layer plasma. Shielding efficiency is higher for aluminum than for carbon. Shielding action is also observed in a conventional tokamak.

(4) Divertor effects on plasma confinement

The divertor increases the energy-confinement time by a factor of 2.5 by reducing the radiation loss and broadenning the electron temperature profile. The divertor does not affect on ion temperature, particle-confinement time and heat diffusion coefficient.

(5) Characteristics of a scrape-off layer plasma

The particle flow velocity is a few times less than the sound velocity, heat transmission rate is consistent with a sheath model and the particle diffusion coefficient is about ten times less than the Bohm diffusion

coefficient. An empirical scaling low for the electron temperature is obtained and gives an extremely high temperature for the edge plasma or the scrape-off layer plasma in a large tokamak without any edge cooling method.

(6) Particle-confinement time

An empirical scaling low for the average particle-confinement time is obtained and is similar to that of the energy-confinement time. The radio of the average particle-confinement to energy-confinement time is 1.5 without the divertor and 0.8 with the divertor. Confinement time of metallic and gaseous impurities is comparable to the average particle-confinement time.

(7) Impurities

Pseudo continuum is observed in a range of 45-200 $\overset{\circ}{A}$ and has an internal structure, i.e. the radial intensity profile has the peak at the plasma center with T_{eo}=700 eV at short wavelength ($\lesssim$100 $\overset{\circ}{A}$) and at r=4-5 cm or $T_e \gtrsim 200$ eV at longer wavelength ($\gtrsim$100 $\overset{\circ}{A}$). The radiation loss due to the pseudo continuum is comparable to that due to oxygen impurity. Oxygen content is 2 % and gold content is roughly estimated 0.05 %.

(8) Origin of metallic impurities

Ion sputtering, arcing and evaporation are identified and sputtering by impurity ions is the dominant process of metallic impurity release at a limiter or a neutralizer plate in a stable discharge.

The results demonstrate the important divertor actions and improvement of plasma characteristics by the divertor. Ion sputtering is important in a future large tokamak as well as in the present day tokamak. Some methods to control the edge plasma at a low temperature are necessary in a large tokamak. If the edge cooling is not sufficient, the divertor allows the edge plasma with a somewhat higher temperature by reducing impurity influx into the main plasma and has to be useful also to control the edge plasma. Impurity transport in a scrape-off layer plasma is very important even in a conventional tokamak because the impurity influx into the main plasma is ruled not only by impurity production rate but also by the impurity transport in the scrape-off layer plasma. The experimental results of scrape-off layer plasmas and shielding actions offer data from which we can discuss the impurity control over a wide range of plasma parameters if we know detailed data of sputtering not only by fuel- and α-particles but also by impurity ions.

Acknowledgements

* DIVA Group

Arrangement	Y. Shimomura
	H. Maeda
Fluctuation	K. Odajima
	H. Kimura
Impurity Injection	M. Nagami
	T. Yamauchi
	S. Sengoku
MHD Equilibrium and Stability	S. Yamamoto
	S. Sengoku
Microwave Interferometory	A. Funahashi
	K. Takahashi
	A. Nagashima
Neutral Particle Energy Analysis	H. Takeuchi
	K. Takahashi
Plasma-Wall Interactions	H. Maeda
	H. Kimura
	H. Ohasa
	H. Ohtsuka
	S. Yamamoto
Radiation Loss and Power Balance	H. Maeda
	K. Odajima
	H. Ohasa
Runaway Electron	S. Yamamoto
	S. Sengoku
Scrape-off Layer Plasma	H. Kimura
	K. Odajima
	H. Ohtsuka
	S. Sengoku
Spectroscopy	S. Kasai
	T. Sugie
	M. Shiho
	M. Nagami
Soft-X Ray	K. Kumagai
Surface Observation	H. Ohtsuka
	T. Arai
Thomson Scattering	T. Yamauchi
	K. Kumagai
	S. Sengoku
Computer Simulation	M. Azumi
	M. Nagami
Operation and Engineering Group of DIVA	K. Anno
	T. Shibata
	T. Arai
	H. Hiratsuka
	H. Sunaoshi

Appendix I. Heat Flux to Material Surface**

This appendix describes the experimental study on the thermal interaction between the plasma and the walls in the divertor tokamak, DIVA[1)~6)].

It is well known that a sheath potential built up in front of an electrically insulated conducting plate plays an important role for a thermal barrier. Heat flux q (watts/cm^2) to an electrically insulated conducting plate in a plasma is written as follows[7)].

$$q = \gamma I_s \cdot T_e \qquad\qquad (a-1)$$

where I_s (A/cm^2) is ion saturation current density, T_e (eV) is electron temperature and γ is called as a heat transmission rate, and $\gamma=7.8$ for hydrogen plasma of $T_e=T_i$, where T_i is proton temperature.

In the scrape-off layer of DIVA various types of probes has been successfully used[8)]. The procedures of the present experiment is to measure the local values of q, I_s and T_e with pertinent probes scanned in the divertor region and to calculate γ. As noted in previous experiments[3),5)], heat fluxes in the divertor are highly asymmetric as to the median plane and high energy electrons escaping from the main plasma cause this asymmetory, since they can exist in one side of the divertor until they annihilate at the neutralizer plate. Hereafter we distinguish each side of the divertor as to the median plane as an electron side and ion side of the divertor, respectively. In the electron side, γ is a few to ten times larger than the value estimated by Eq.(a-1). Moreover even in the case with additional hydrogen gas injection after starting the discharge, γ is a few times larger than expected, although the amount of high energy electrons is considerably reduced. However the above experiments were somewhat limited in accuracy. The thermocouple used for heat flux measurement had a response time of 5 ms, which is too large for our experiment, since in this time interval ion saturation current and electron temperature change considerably. In addition, the use of a Langmuir probe for the measurement of I_s and T_e may be difficult particularly in the presence of high energy electrons.

We now report results with our recently developed thin-film thermometer[9),10)] with a response time 0.2 ms, which is small enough for our experiment. As for a particle measurement, an electrostatic multigrid energy analyzer is used, which is able to measure I_s and T_e even in the presence of high energy electrons.

From detailed measurement with these probes, the relationships between heat flux q, heat transmission rate γ and other plasma parameters are obtained. It is found that the thermal interaction between the plasma and the walls in the scrape-off layer can be described by a simple sheath model. These results can be applied to the thermal interaction between the plasma and the limiter in the scrape-off layer of a conventional tokamak[11].

A.1. Thermometer and Multi-grid Energy Analyzer

The detailed description of the thin-film thermometer is given elsewhere[9],[10]. Here it is briefly described. Figure A-1 shows the structure of the thermometer. The backing metal was a thin molybdenum plate of 8 × 12 mm^2 area and 0.1 mm thickness. Silicon monoxide was vacuum-deposited on the molybdenum plate and then nickel. The silicon monoxide layer served as an electrical insulator. The temperature of the molybdenum was measured by the resistance change of the nickel film. The response time of the thermometer was measured using a Q switched pulse laser and was found to be less than 0.2 ms.

The width of the nickel film is 0.4 mm which is much larger than the thickness of the molybdenum plate. Thus the spatial resolution of the thermometer is determined by the width of the nickel film.

Figure A-2 shows the multigrid energy analyzer schematically. The external jacket of the analyzer is at the same potential as the vacuum vessel. In front of stainless steel collector plate C, 5 mm in diameter, three stainless steel grids (E, G_1, G_2) are placed at 1 mm spacings. The grid E with the same potential as the vacuum vessel has seven holes, 100 μm in diameter and 100 μm long, in 1 mm aperture, which decides a spatial resolution of this analyzer. The mesh grids G_1 and G_2 are of 20 and 50 μm wires and have a transparency of 0.31 and 0.44, respectively.

Figure A-2 also shows potential distributions between three grids and a collector plate to obtain ion and electron velocity distributions. Ion saturation currents are obtained by the following procedure, which discriminates against high energy and secondary electrons. That is, we adopt the potential profile shown in Fig. A-2-a and subtract the collector signal at +150 V from that at -40 V. The latter consists of ion saturation current plus electron leakage current, the former consists of electron leakage current only, where the term "electron leakage current" applies to the electrons which have higher energy than the retarding potential of grid

G_2 and succeed in passing grids G_1 and G_2, in addition to those which are emitted at grid G_2 and can reach collector C. It was experimentally confirmed that the electron leakage current is independent of the collector potential unless it is less than the critical potential which is equal to G_2 potential plus the mean energy of secondary electrons.

A.2. Experimental Results

Figure A-3 shows cross-sectional view of DIVA. The experiment was performed under the following operational conditions. The toroidal magnetic field was fixed at 1 T. The ratio of the divertor hoop current to the plasma current was 1.2, where the latter was 14 kA with a flattop. The base pressure was 1×10^{-7} torr, and hydrogen gas of 1.5×10^{18} atoms was admitted by four fast-acting valves 0.8 ms before starting a discharge. Additional hydrogen gas was injected 2.2 ms after starting the discharge at a rate of 1.7×10^{19} H_2/s. Central electron and ion temperatures were 200 and 80 eV from laser scattering and charge exchange neutrals, respectively. Average electron density was 1×10^{13} cm^{-3} from a 4 mm μ-wave interferometer.

A thermometer and a multigrid analyzer were scanned vertically at R=40 cm.

Figure A-4 shows typical thermometer data. This figure represents resistance change of Ni thin-film. The temperature T of the thin-film, which is assumed to be equal to that of the molybdenum plate, is obtained from a calibration curve. If heat flux to the divertor has a very sharp peak in space, we must take heat conduction in the molybdenum plate into account to calculate heat flux from the measured temperature[10].

Figure A-5 shows the Z-profile of heat flux calculated taking above effect into account in the electron side of the divertor. This profile indicates a sharp peak near Z=45 mm. In this figure the results from a simple heat balance equation,

$$q(Z,t) = \rho cd \frac{dT(Z,t)}{dt} \qquad (a-2)$$

where ρ, c, and d are density, specific heat and thickness of the molybdenum backing plate, respectively, are also shown.

It is found that the peak value of heat flux would be underestimated by a factor of 1.5 if Eq.(a-2) were used. However it is only narrow region, $\Delta Z \simeq 1$ mm, that the influence of transverse heat transfer is prominent.

Outside this region both results from the simple heat balance equation and the transverse heat conduction equation are in good agreement.

Next, we describe the results of particle measurements. Figure A-6 shows time variation of electron energy spectra at Z=45 mm. These spectra were obtained changing the bias voltage of grid G_2 of the multigrid analyzer shot by shot. It was found that relatively high energy electrons, whose energy range is 100 to 200 eV, exist in a narrow layer on the electron side of the divertor, i.e. Z=45∿50 mm and that amount of these electrons varies with time. In order to examine a much higher range of energy than that of the multigrid analyzer, we scanned an X-ray target[12], whose spatial resolution is 1 mm, on the electron side of the divertor. The X-ray energy observed with 100% efficiency ranges approximately from 10 to 100 keV, as determined by the thickness of the aluminum window and the NaI scintillator. Figure A-7 shows Z-profile of X-ray intensity I_x from the target. The profile of electron flux whose energy is larger than 150 eV is also depicted in this figure. The peak position of I_x is 42.5 mm, where the heat flux is much smaller than that of Z=45.0 mm. It is clear that the peak heat flux has no correlation with runaway electrons, and that the peak position rather coincides with the path of the electrons in 100 – 200 eV range of energy.

The measurement of ion saturation current density was also made by the procedure described in the previous section. Ion saturation current density and bulk temperature of electrons are shown in Fig. A-5. It is noted here that measured heat flux is factor 2∿3 larger than the values calculated from Eq.(a-1) using measured ion saturation current density and bulk temperature of electrons.

A.3. Discussions and Conclusions

It is natural that this relatively large heat flux is due to the electrons in 100-200 eV range of energy. Hereafter we call those the epithermal electrons. The loss mechanism of the epithermal electrons from the main plasma column is discussed in Ref. (12). To confirm the relationship between heat flux and epithermal electrons we make some simple analysis following Lovberg[7]. We assume electron velocity distribution as a two component Maxwellian. That is,

$$n_e = \sum_{k=1}^{2} n_{ek} \left(\frac{m}{2\pi T_{ek}} \right)^{\frac{1}{2}} \exp\left(-\frac{mv^2}{2T_{ek}} \right) \tag{a-3}$$

where n_e and m are the density and mass of electrons and suffixes 1 and 2 refer to low and high energy components, respectively. Furthermore we make two assumptions. 1) Ion temperature T_i is equal to T_{el}. This fact was roughly assured in the scrape-off layer by a multi-grid analyzer. 2) Secondary electrons are emitted from the backing plate of the thermometer. These are induced only by electron impact. The secondary electron emission coefficient on a molybdenum surface, δ (electrons/electron), is referred from Ref.(13). The data in Ref.(13) are given for monoenergetic electrons. In the present analysis, however, we adopt the mean energy for the incident energy of primary electrons. This treatment seems to be correct, because δ can be derived from Eq.(a-4) if the potential difference between the plasma and the electrically insulated plate is known, and it is experimentally confirmed that δ so obtained is in good agreement with the data in Ref.(13) for various plasma parameters i.e. $T_e = 20 \sim 50$ eV.

Ion induced secondaries are not considered here because the secondary electron emission coefficient due to ion impact on a molybdenum surface is much smaller than that due to electron impact in the energy range considered.

A floating potential ϕ_o of a backing plate, where a space potential is set to be zero, can be determined by the condition that net current to this plate is equal to be zero. That is,

$$\sum_{k=1}^{2} \frac{1-\delta_k}{4} n_{ek} \left(\frac{8T_{ek}}{\pi m}\right)^{\frac{1}{2}} \exp \frac{e\phi_o}{T_{ek}} = \frac{\xi}{4} n_o \left(\frac{8T_i}{\pi M}\right)^{\frac{1}{2}} \tag{a-4}$$

where n_o is ion density, M is ion mass and ξ is a correction factor of electron to ion saturation current ratio in a strong magnetic field. ξ was measured by a plane probe for the scrape-off layer plasma in DIVA and has a value, $2 \sim 4$. Typical data for T_{el}, T_{e2}, corresponding secondary emission coefficients δ_1, δ_2 and n_{el}/n_o at Z=45 mm, t=20 ms are 55 eV, 198 eV, 0.59, 0.98 and 0.083, respectively. Calculated ϕ_o using $\xi=3$ at 20 ms is shown in Fig. A-7. Heat flux to the thermometer is written as

$$q = I_s T_{el} \left[\frac{2}{\xi} \cdot \sqrt{\frac{M}{m}} \left\{ (1-\varepsilon) \exp\frac{e\phi_o}{T_{el}} + \varepsilon h^{\frac{3}{2}} \exp\frac{e\phi_o}{T_{e2}} \right\} + 2 - \frac{e\phi_o}{T_{el}} \right] \tag{a-5}$$

where $h = T_{e2}/T_{el}$, $\varepsilon = n_{e2}/n_o$ and $I_s = \frac{1}{4} n_o \left(\frac{8T_i}{\pi M}\right)^{\frac{1}{2}}$.

This may be compared with heat flux in the absence of high energy tail,

by rewritting in the form

$$q = F \cdot \gamma \cdot I_s T_{el} \tag{a-6}$$

$$\gamma = 2\left(\frac{1}{1-\delta_1} + 1\right) - \ln \frac{\xi \sqrt{\frac{m}{M}}}{1-\delta_1} \tag{a-7}$$

where γ is the heat transmission rate in the absence of the high energy tail, equal to $6.7 \sim 8.6$ for hydrogen plasma with $T_{el}=7-55$ eV and $\xi=3$, and F is the correction factor for the two component model.

For the parameter range of the present experiment, i.e. $h \lesssim 4.0$ and $\varepsilon \lesssim 0.1$, the low energy term in the left hand side of Eq.(a-4) is dominant. In this case $e\phi_o$ and F are approximately written as follows.

$$e\phi_o \simeq T_{el} \ln \frac{\xi \sqrt{\frac{m}{M}}}{(1-\delta_1)(1-\varepsilon)} \tag{a-8}$$

$$F \simeq \frac{1}{\gamma}\left[2\left(\frac{1}{1-\delta_1} + 1\right) + \frac{2}{\xi}\sqrt{\frac{M}{m}} \, \varepsilon h^{\frac{3}{2}}\left\{\frac{\xi \sqrt{\frac{m}{M}}}{(1-\delta_1)(1-\varepsilon)}\right\}^{\frac{1}{h}} - \frac{e\phi_o}{T_{el}}\right] \tag{a-9}$$

These approximate forms of $e\phi_o$ and F are in agreement with the exact value from Eq.(a-4) and (a-5) within 10% using the measured values of h and ε. Before the comparison between theory and experiment we estimates the accuracy of the experimental data of the heat flux.

Transverse heat transfer in the backing plate of the thermometer was already discussed in Sec. A-2. Another probable error for the measurements is due to the fact that the floating potential of the backing plate of the thermometer is shallower than expected from Eq.(a-4), since the dimension of the backing plate, 8 mm, is larger than the characteristic length for spatial variation of the floating potential.

If the bias voltage of the thermometer is shallower than the local floating potential, the heat flux is larger than that of a plate at local floating potential. In order to confirm this, the dependence of heat flux on the bias voltage of the sheath of a thermocouple whose diameter is 0.25 mm was examined. Figure A-8 shows time integrated heat flux to a thermocouple as a function of bias voltage with respect to the vacuum chamber.

In this figure probe characteristics are also depicted. These were obtained by employing a sheath, which is made of stainless steel, of the thermocouple as an electrode.

Transient heat flux as a function of bias voltage ϕ is given by sub-

stituting ϕ instead of ϕ_o in Eq.(a-5). It is with this equation that the time integrated heat flux shown in Fig. 8 is compared, although rigorous comparison would be rather inadequate, since both electron temperature and ion saturation current change temporally during the discharge.

The minimum heat flux is obtained by the condition $\frac{dq}{d\phi}\big|_{\phi=\phi_m} =0$, that is

$$e\phi_m = T_{el} \ln \frac{\xi}{2}\sqrt{\frac{m}{M}} \qquad (a-10)$$

, assuming $\varepsilon=0$ for simplicity.

The floating potential, setting a secondary electron emission coefficient to be zero, is given below.

$$e\phi_o = T_{el} \ln \xi \sqrt{\frac{m}{M}} \qquad (a-11)$$

The difference between the two potentials $\phi_o-\phi_m$ is about $0.7\,T_{el}/e$, using $\xi=6.4$ from the probe characteristics shown in Fig. 8. This is consistent with the experiment, where the minimum heat flux is realized in the vicinity of $e\phi=e\phi_o - T_e$.

Let us estimate how much the heat flux measurement was affected by the above mentioned effect. For example we consider the peak heat flux at t = 20 ms (see Fig. A-5). The calculated local floating potential is -94 V. In this case $q=18.5\,I_s T_{el}$, where $\xi=3$ is assumed. The floating potential of the backing plate of the thermometer placed at Z=45 mm can be calculated by the equation integrating Eq. (a-4) from Z=41 mm to Z=49 mm, and is about -85 V. By Eq.(a-5) q becomes $19.8\,I_s T_{el}$. From this result it can be said that the heat flux measurement was affected within 10% because the thermometer was not at local floating potential, and that the influence of this effect is relatively small. We are now in a position to make a comparison between theory and experiment.

Figure A-9 shows the relationship between heat flux q measured on the electron side of the divertor and correction factor F calculated exactly from Eqs. (a-4) and (a-5) using experimental data for h and ε, and $\xi=3$.

Heat fluxes are averaged in space over the aperture of the multigrid analyzer. The error bars for q are so determined as to include the widest range between the shot-to-shot deviations and the temporal changes for the neighbouring time steps, $\Delta t=\pm1$ ms. The error bars for F are due to

ambiguity of ξ. The upper values correspond to $\xi=2$, the lower ones corresponding to $\xi=4$. The values of q corresponding to F=1 are those in the absence of epithermal electrons. It is seen that there is a strong correlation between the relatively large heat flux and the presence of epithermal electrons.

The relationship between heat flux q measured and $F\gamma I_s T_{el}$ is shown in Fig. A-10. As a whole they are in good agreement.

The present experiment was performed under the discharge condition with an additional gas injection. Relatively large heat flux on the electron side of the divertor has a strong correlation with epithermal electrons whose energy range is 100 to 200 eV, and has no correlation with runaway electrons. If the amount of additional gas was increased, the number and kinetic energy of epithermal electrons became small. Hence heat flux was also relatively small.

On the contrary, in the case of no additional gas injection, the heat flux becomes very large.

The peak values of heat flux at 15 ms for three additional gas injection rates are tabulated in Table A-1.

Table A-1   Comparison between peak values of heat flux
for different additional gas injection rates

Rate of an additional gas injection	Peak values of heat flux
0 H_2/s	2200 Watts/cm^2
1.7×10^{19}	330
4.5×10^{19}	180

Thermal interaction between the plasma and an electrically insulated plate in the divertor region of DIVA, where $T_e \lesssim 50$ eV and $n_e \lesssim 1 \times 10^{12} cm^{-3}$, was experimentally investigated. Results show that the heat flux to the divertor is calculated from a simple sheath model including secondary electron emission effects even if epithermal electrons are present. This results can be applied to the thermal interaction between the plasma and the limiter in a conventional tokamak.

References

** Kimura, H., et al., to be published in Nuclear Fusion

1) Maeda, H., et al., Proc. Int. Symp. on Plasma Wall Interaction, Jülich, Germany, (1976) 537.

2) Maeda, H., et al., 6th Conf. on Plasma Physics and Controlled Nuclear Fusion Research, Berchtesgaden 1976, paper IAEA-CN-35/A-18.

3) Shimomura, Y., et al., Proc. 7th Europ. Conf. on Controlled Fusion and Plasma Physics, Lausanne, 2 (1975) 81.

4) Shimomura, Y., et al., Phys. Fluids 19 (1976) 1635.

5) Maeda, H., et al., Nucl. Fusion 16 (1976) 148.

6) Ohasa, K., et al., submitted to Nucl. Fusion

7) Lovberg, R.H., "Plasma Diagnostic Techniques" (R.H. Huddlestone and S.L. Leonard, ed.) Chap. 3 Academic Press New York (1965).

8) Kimura, H., et al., "Diagnostics of a Scrape-off Layer Plasma", Japan Atomic Energy Research Institute Report JAERI-M 6971 (1977).

9) Ueda, N., et al., "Development of a Heat Flux Meter and Measurement of the Heat Flux to the Divertor in DIVA" Japan Atomic Energy Research Institute Report JAERI-M 6723 (1976).

10) Seki. M., et al., J. of Nuclear Science and Technology 14 (1977) 534.

11) Gomay. Y., et al., to be published in Nucl. Fusion.

12) Yamamoto, S., et al., to be published in Nucl. Fusion.

13) Barnett, C.F., et al., "Atomic Data for Controlled Fusion Research", Oak Ridge National Laboratory Report ORNL-5207 (1977).
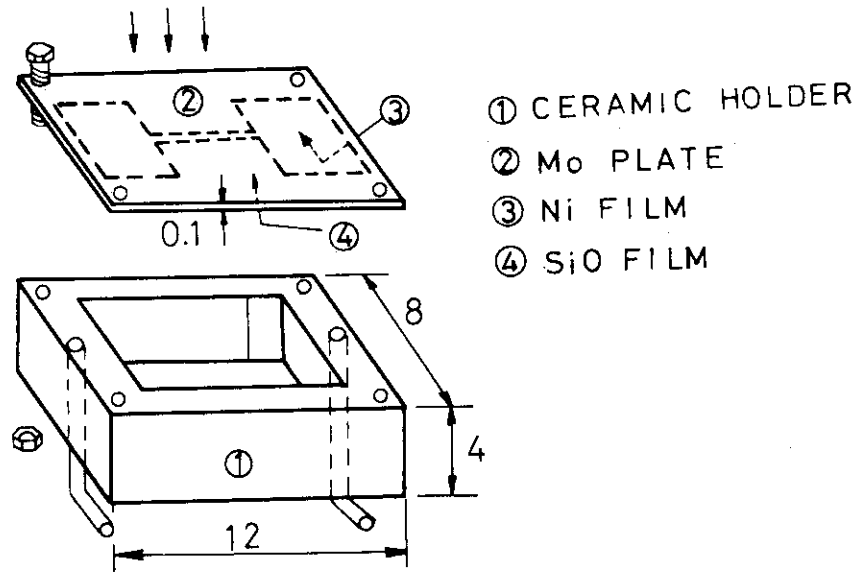
Fig. A-1 Schematic drawing of the thermometer.

(a)

(b)
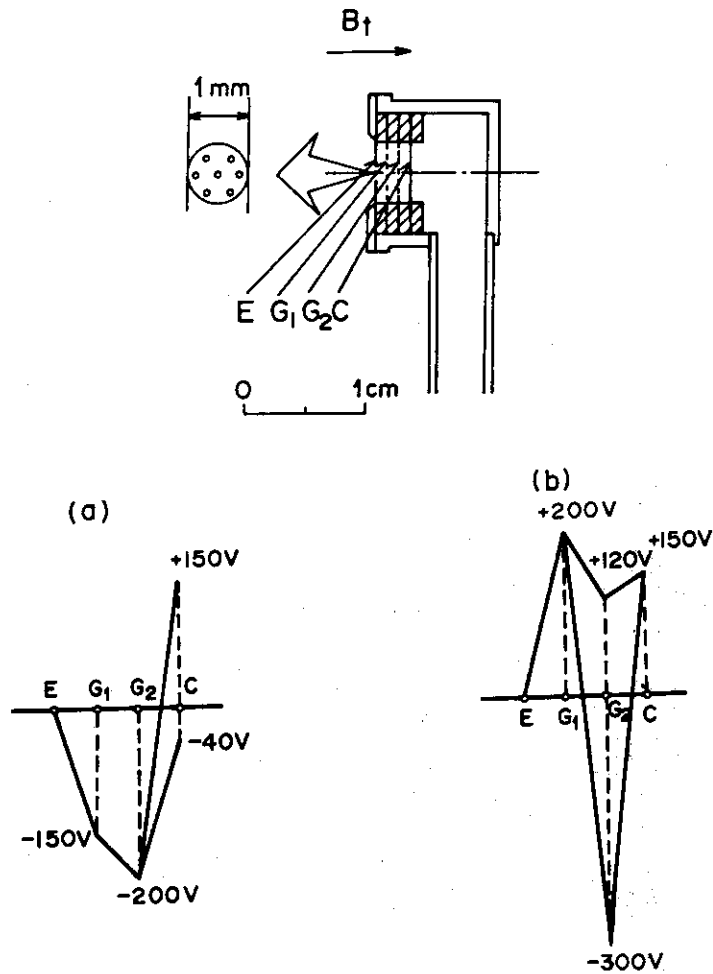
Fig. A-2 Schematic drawing of the electrostatic multigrid energy analyzer and potential distribution between the grids E, G_1, G_2 and the collector C for (a) ion and (b) electron energy analysis.
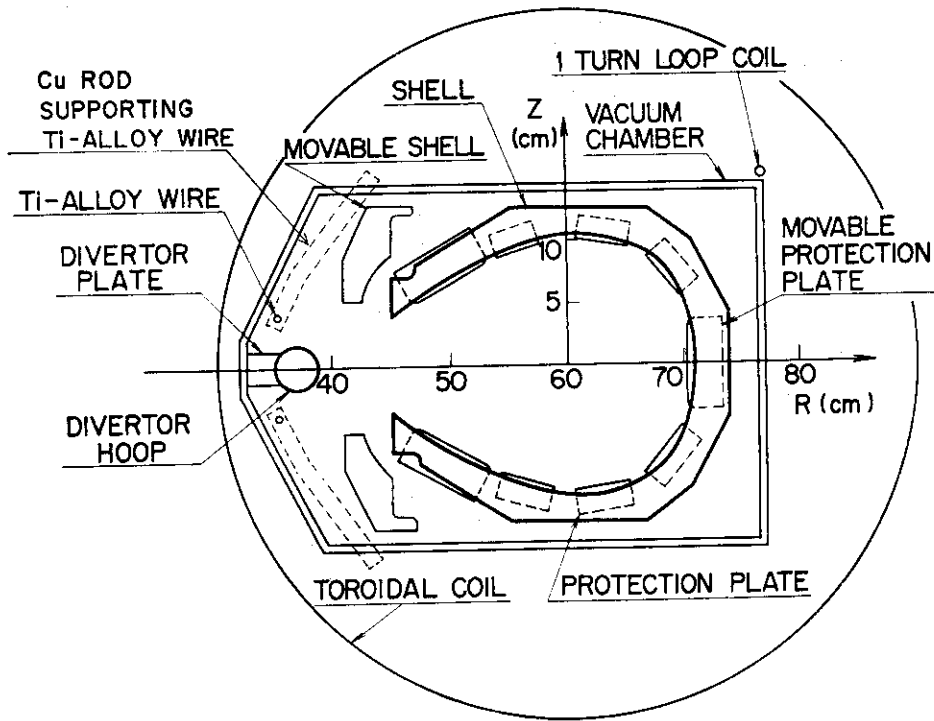
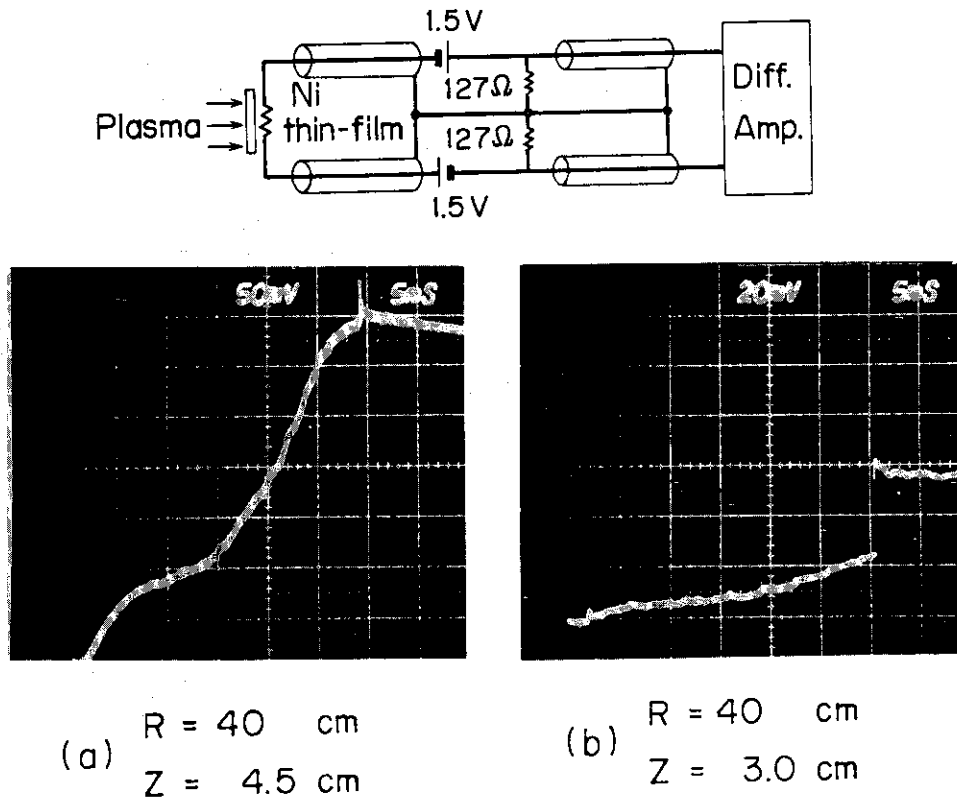Fig. A-3   Cross-sectional view of DIVA.

(a)   R = 40   cm
       Z =   4.5 cm

(b)   R = 40   cm
       Z = 3.0 cm

Fig. A-4   Outputs of the thermometer located at different positions.

Fig. A-6 Energy spectra of electrons on the electron side of the divertor.

Fig. A-5 Z-profiles of heat flux q, electron temperature T_e and ion saturation current density I_s on the electron side of the divertor. Heat fluxes near the peak position are corrected by the transverse heat conduction equation.
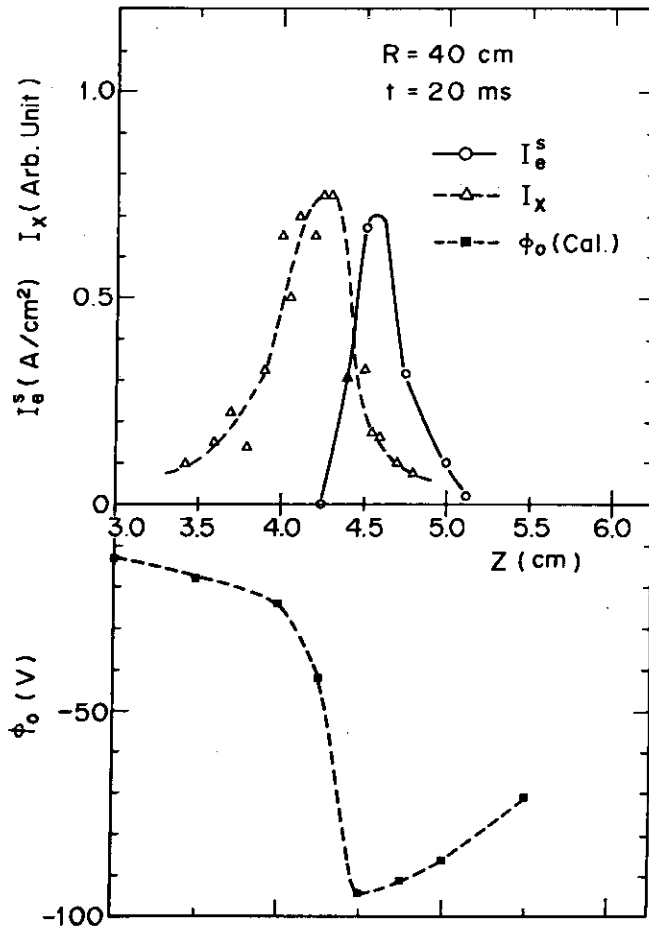
Fig. A-7 Z-profiles of epithermal electron flux I_e^s, X-ray intensity I_x and calculated floating potential ϕ_o on the electron side of the divertor.
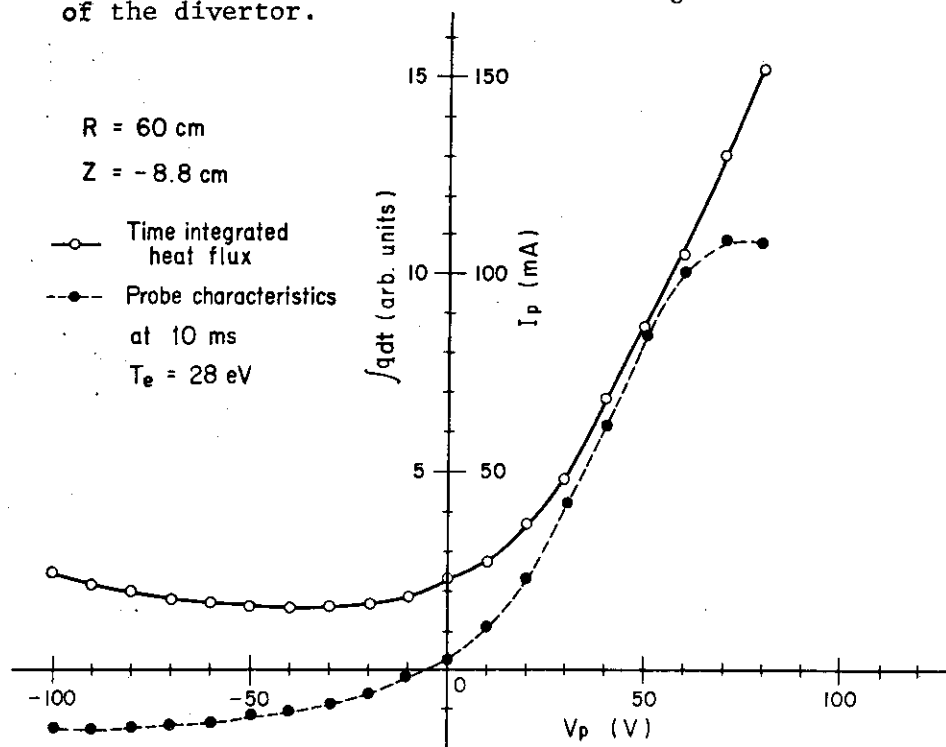
Fig. A-8 Time integrated heat flux in the whole discharge duration to a thermocouple as a function of a bias voltage V_p of a sheath of the thermocouple, together with the probe characteristic at 10 ms employing the sheath as an electrode.
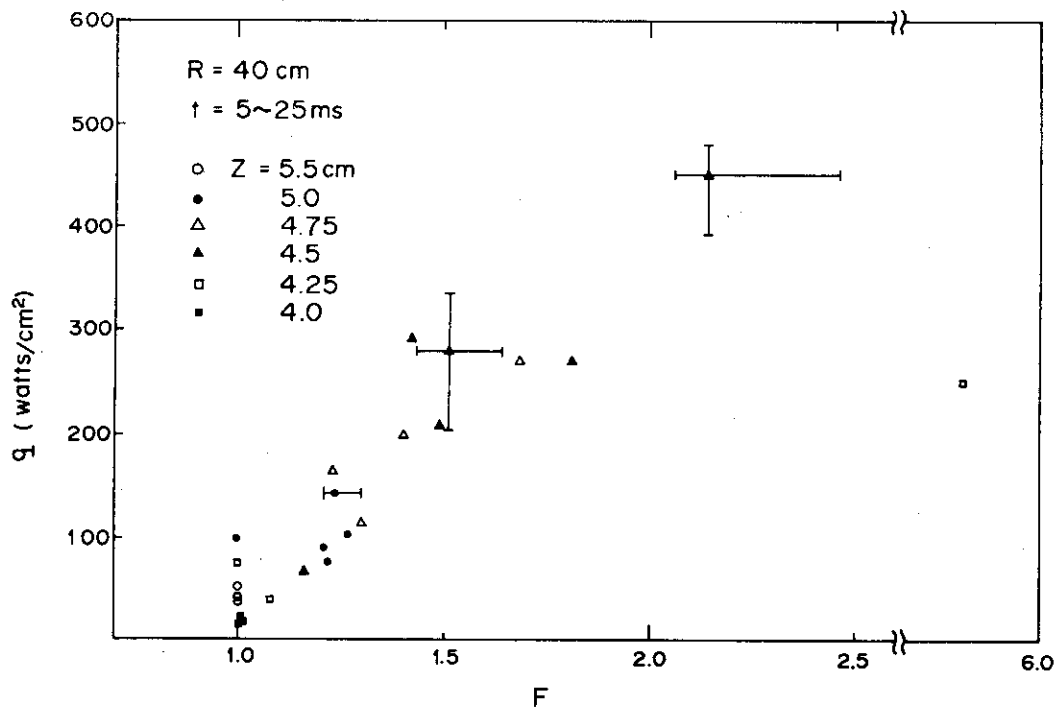
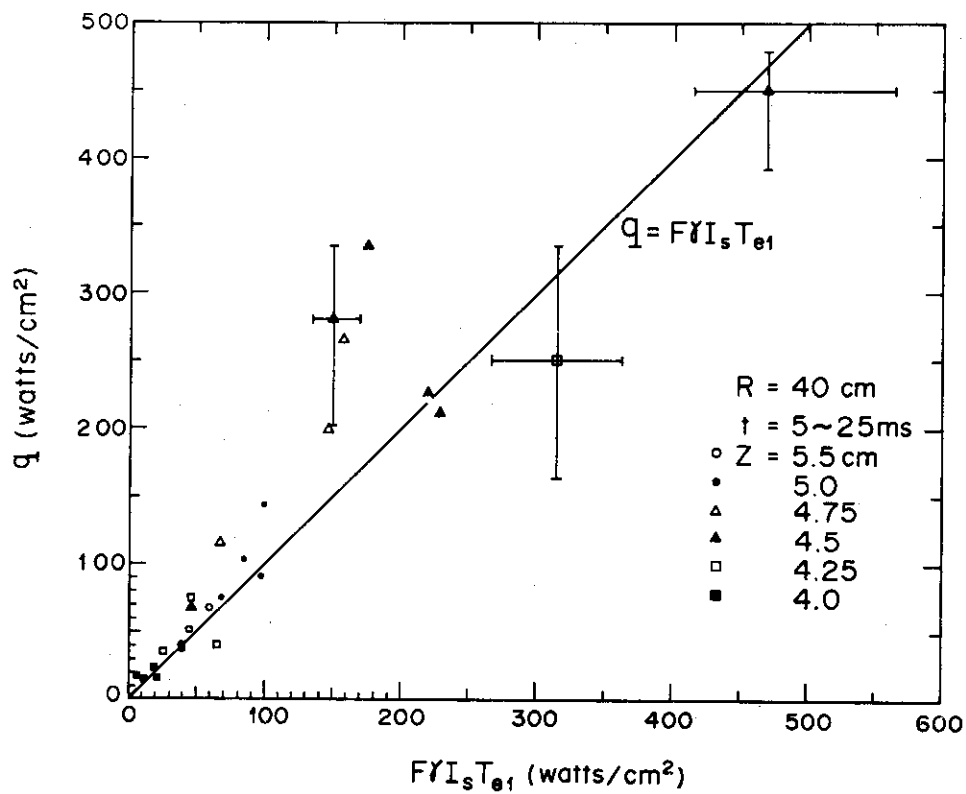Fig. A-9 Relationship between heat flux q and correction factor F for the two component model.

Fig. A-10 Relationship between heat flux q and $F\gamma I_s T_{e1}$ for the two component model.

Appendix II. Pseudo continuum in a Low Current Discharge***

In the previous experiment with $B_T=1$ T, $I_{p_0}=14$ kA and $T_{eo}=250$ eV. The pseudo continuum was observed in a range of 120 Å - 250 Å as shown in Fig. A-11. The radiation loss power was ruled by the pseudo continuum because the low-z impurities could be neglected. Relation between the total radiation loss including charge-exchange loss and the radiation loss due to the pseudo continuum was shown in Fig. A-12.

*** Shiho, M., et al., Japan Atomic Energy Research Institute Report
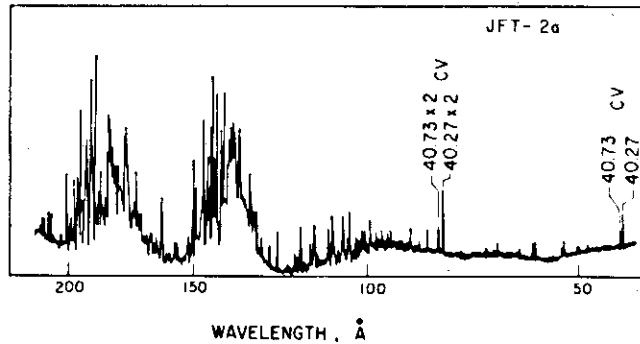   JAERI-M 7397 (1977)

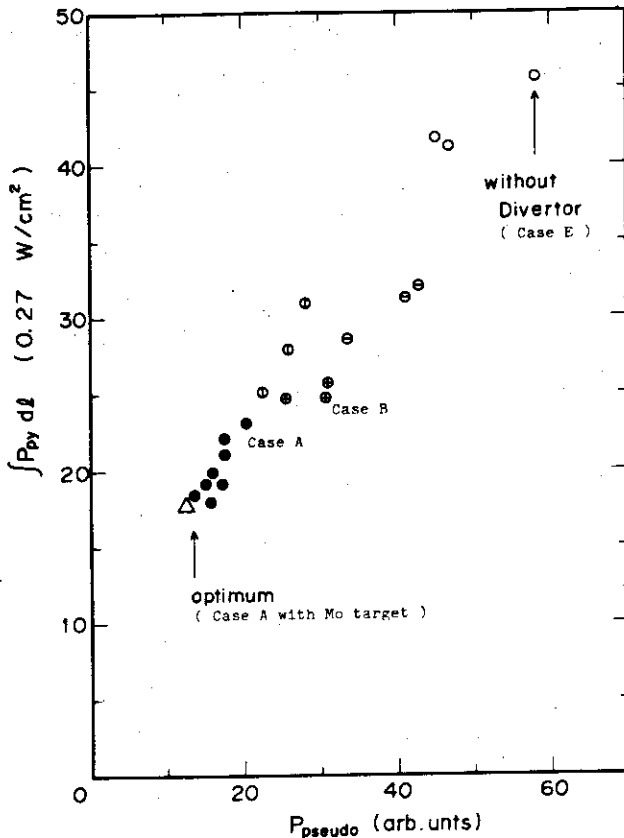Fig. A-11   Intense emission lines from the DIVA plasma.

Fig. A-12

A correlation between the radiative power measured by pyroelectric detector and that of the pseudo continuum. Closed and open circles represent the cases of with and without divertor, and the triangle is the optimum condition.